Investigation of Tungsten Surface Effects under High Heat Flux Conditions

John R. Echols

Thesis submitted to the Faculty of the

Virginia Polytechnic Institute and State University

in partial fulfillment of the requirements for the degree of

Master of Science

in

Materials Science and Engineering

Leigh Winfrey, Chair

Céline Hin

William Reynolds

November 21, 2014

Blacksburg, Virginia

Keywords: Fusion, Nuclear Materials, Plasma Facing Components, Electrothermal Plasma

Investigation of Tungsten Surface Effects under High Heat Flux Conditions

John R. Echols

(ABSTRACT)

Material erosion, melting, splashing, bubbling, and ejection during disruption events in future large tokamak reactors are of serious concern to component longevity. The majority of the heat flux during disruptions will be incident on the divertor, which will be made from tungsten in the future large tokamak ITER. Electrothermal plasma sources operating in the confined controlled arc discharge regime produce heat fluxes in the range expected for hard disruptions in future large tokamaks. The radiative heat flux produced inside of the capillary discharge channel is from the formed high density (10^{23}-$10^{27}/m^3$) plasma with heat fluxes of up to 125 GW/m^2 over a period of 100s of μs, making such sources excellent simulators for ablation studies of plasma-facing materials in tokamaks during hard disruptions.

Experiments have been carried out with the PIPE device exposing tungsten to these high heat flux plasmas. SEM images have been taken of the tungsten surfaces, cross sections of tungsten surfaces, and ejected material. Melting and bubble/void formation has been observed on the tungsten surface. The tungsten surface shows evidence of melt-layer flow and the existence of voids and cracks in the exposed material. The ejected material does not show direct evidence of liquid material ejection which would lead to splashing. EDS analysis has been performed on the ejected material which demonstrates a lack of deposited solid tungsten particulates greater than micron size.

Dedication

I would like to dedicate this work to my parents, Jim and Elaine, who always encouraged my love of learning. Without their patience for the many conversations I started and continued with "Why?", this work would not exist.

Acknowledgments

I would like to thank my advisor, Dr. Leigh Winfrey, for guiding me to this research and for all she has taught me about fusion. I would like to thank Dr. Céline Hin for her advice and guidance on scientific rigor and Dr. William Reynolds for his insightful discussions when I was at a loss to explain phenomena. I would finally like to thank Dr. Mohamed Bourham for his tireless and enthusiastic guidance with the PIPE device.

I would also like to thank Virginia Tech's Nuclear Engineering Program, Department of Mechanical Engineering for providing the funding for this research.

Contents

List of Figures

List of Tables

Chapter 1

Introduction

1.1 Fusion and Tokamak Reactors

The production of energy by nuclear fusion can be achieved through the fusion of atoms of light elements. The energy released in these reactions is equal to the difference in mass between the two light elements and the single fused nucleus. This energy is carried by the daughter particle(s) in the form of kinetic energy. There are a number of reactor designs and fuel mixtures currently under investigation which intend to lead to commercial energy production. One of the most promising paths is the fusion of deuterium and tritium, two isotopes of hydrogen, in a tokamak reactor.

Several roadmaps[1,2] with the end goal of power producing tokamak reactors are under consideration. Large-scale tokamak reactor experiments are critical to the success of these

plans. The Joint European Torus (JET) is currently the largest fusion experiment in the world. This distinction will pass to ITER (latin for *the way*) in 2020 when operation is planned to begin. A demonstration power plant (DEMO) is expected to follow ITER and is intended to be the first fusion plant to generate electrical power. There is a possibility another large tokamak will be operated between ITER and DEMO.

High temperature plasmas such as those which are used in tokamak reactors typically report temperatures in electronvolts (eV) per Boltzmann constant. The Boltzmann constant is commonly dropped to simply use eV. Tokamak reactors are designed to magnetically confine a plasma of fuel elements at temperatures greater than 10keV. ITER is expected to have a plasma temperature of around 13keV [3,4]. For comparison, the core of the sun has a plasma temperature of about 1.4keV. A tokamak consists of a toroidal vacuum vessel surrounded by magnetic field coils. A solenoid runs through the center of the torus. The geometry of a tokamak is described in terms of toroidal and poloidal directions. As shown in Figure 1.1, the toroidal direction describes a vertical loop around the torus and through the center. The poloidal direction describes the horizontal loop traveling the entire torus. The torus is also described in terms of major and minor radii. The major radius is the distance from the center of the tube to the center of the torus, and the minor radius is the radius of the tube.

To achieve fusion, positively charged nuclei must be brought close enough that the strong force overtakes the coulomb repulsion. Tokamak reactors achieve fusion by the confinement and compression of plasmas in the poloidal and toroidal directions. A system of

Figure 1.1: On this torus the blue line represents the toroidal direction and the red line represents the polodial direction. ([5] http://en.wikipedia.org/wiki/Torus#mediaviewer/File:Toroidal_coord.png, 2014, Creative commons 2.5)

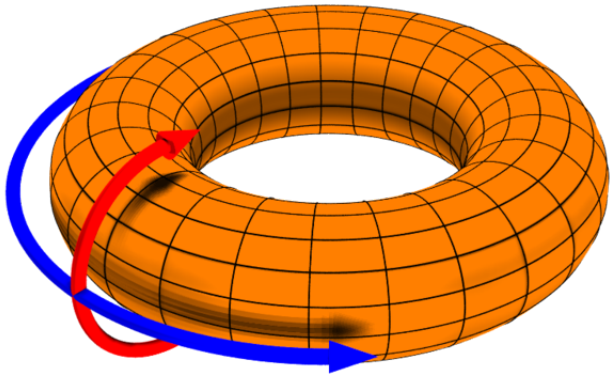

large electromagnets shape the magnetic field in the toroidal direction. A second set of electromagnets induce a current inside the plasma, creating a poloidal field.

Deuterium and tritium are isotopes of hydrogen with one and two neutrons respectively. Deuterium-tritium (DT) fission occurs as follows:

$$ {}^{2}_{1}D + {}^{3}_{1}T \rightarrow {}^{0}_{1}n[14.1MeV] + {}^{4}_{2}He[3.5MeV] \tag{1.1} $$

The released energy is taken advantage of in two ways. The alpha particle heats the DT fuel mixture, sustaining the reaction. The electrically neutral neutrons exit the magnetic confinement and provide useable energy to the first wall of the tokamak. The amount of

Figure 1.2: Comparison of the major and minor radii of ITER and JET. ([6] http://ec.europa.eu/research/energy/euratom/index en.cfm?pg=fusionion=prep- iter. 2014. Reuse is authorized by the European Union website.)

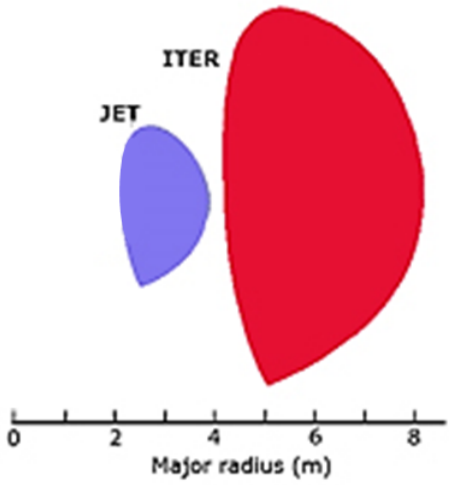

energy which can be generated by a power plant depends, in part, on the volume of the Tokamak. Figure 1.2 demonstrates the difference in plasma volume between ITER and JET.

The high flux of 14.1 MeV neutrons and high heat fluxes generated in fusion can cause incredible damage to reactor materials. The viability of first wall materials in tokamak reactors is dependent on a number of factors. The materials must be able to withstand the high neutron fluence produced by fusion reactors. They must not become radioactive enough over the use lifetime such that they produce unacceptable amounts of nuclear waste. The material must be selected to minimize plasma contamination, be compatible with intense and fluctuating magnetic fields, and easily allow for the passage of large heat flux. Materials

Figure 1.3: A model of the ITER divertor. ([13] The ITER Divertor. Graphic. ITER.org. http://www.iter.org/mach/divertor. Used under fair use, 2014.)

currently under consideration for use in the first wall include boron carbide, beryllium, graphite, carbon fiber composite, lithium, molybdenum, and tungsten [7-11].

Despite the preferential properties of these materials, there is much work to be done in fusion materials. An early study by Barabash et al.[12] on plasma-facing materials for ITER was performed with beryllium, tungsten, and carbon fiber composite. This study showed erosion of these materials and formation of mixed materials on plasma-facing surfaces during normal and abnormal operating conditions. Other studies have indicated potental surface erosion, melting, boiling, splashing and aerosol formation, and transport issues [14-18].

Figure 1.3 shows the divertor of a tokamak reactor. The divertor is a structure located at the base of the vacuum vessel and is a key component of most tokamak reactors. The device allows for the removal of heat, impurities, and helium ash from the plasma during

operation. Although the divertor is designed to minimize material interaction with the high-temperature core plasma [18], the plasma-facing components are subject to enormous heat flux. The plasma-facing components of the ITER divertor will be constructed of tungsten.

1.2 Disruption Events in Tokamak Reactors

In tokamaks, a disruption event occurs when there is a total or local loss of plasma confinement. In the event of a total loss of confinement, the energy stored in the plasma (both thermal and magnetic) is deposited onto the divertor and first wall of the tokamak. This process is referred to as the termal quench. In ITER, the geometry of the magnetic field and divertor design leads to a shallow impact angle during a disruption event. ITER's thermal quench is expected to last between 0.1 and 10 ms [4,20,21]. Figure 1.4 shows the timescale of the thermal quench for different tokamak experiments. Because these events have the potential to severely damage plasma-facing components, disruption events are a key issue for future large tokamaks. Depending on the duration of the disruption, the predicted time-normalized surface energy loading for ITER is expected to range between 144 MJ $m^{-2}s^{-0.5}$ and 446 MJ $m^{-2}s^{-0.5}$ for the divertor and 5.2 MJ $m^{-2}s^{-0.5}$ and 16.3MJ $m^{-2}s^{-0.5}$ for the first wall. [21,22]

At the divertor, the canditate materials' limit for melting or vaporization is significantly lower than the expected surface energy loads. For tungsten the limit is 40-60 MJ $m^{-2}s^{-0.5}$ [21]. Early studies of ITER indicated disruptions would expose plasma-facing surfaces to heat

Figure 1.4: Comparison of thermal quench times for tokamak reactors with predicted range for ITER. ([20] Mirnov et al, "Chapter 3: MHD stability, operational limits and disruptions," Nuclear Fusion, vol. 39, pp 2330 (1999). Used under fair use, 2014.)

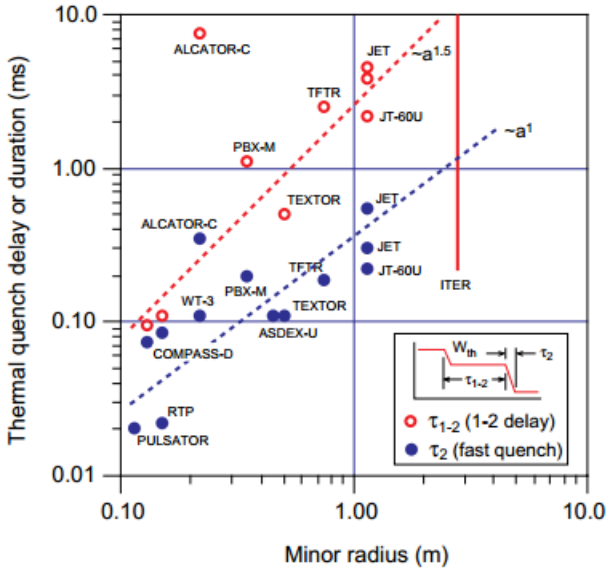

fluxes between 10-100GW/m^2 [4]. More recent studies by Linke et al. [19] have indicated heat fluxes during a disruption greater than 10GW/m^2. The average energy density during disruptions has been shown to scale as R^3, where R is the major radius of the tokamak[23]. From this trend, it is clear that the scaling of surface energy loads will pose a significant challenge for DEMO and future reactors.

1.3 Surface Melting in Off-Normal Plasma Events

In off-normal plasma events such as disruptions, surface melting can lead to a number of problems. Effects such as the generation of aerosols/dust particulates, erosion of material, and material transport in future tokamak reactors is of serious concern. The erosion of material by ablation and change in surface characteristics due to melting can have significant impact on the lifetime of plasma-facing components. Transport of plasma facing material in these scenarios can result in accumulation of activated material. In addition, high-Z particulates from the divertor which are transfered to other first wall surfaces and can inhibit proper functionality.

Figure 1.5 shows limits for tritium and dust in vessel inventories for ITER. Administrative limits are derived from safety limits after taking into account uncertainties of available measurement methods. Mobilisable in vessel dust is composed of free particulates between 100nm and 100μm in size. The erosion of plasma facing materials can produce dust directly or create depositions which can flake to produce dust. A uniform erosion of around 250

Figure 1.5: Safety and administrative limits for tritium and dust in vessel inventories. ([25] Roth, Joachim, et al. "Recent analysis of key plasma wall interactions issues for ITER." Journal of Nuclear Materials 390 (2009): 1-9. Used under fair use, 2014.)

	Safety limits	Administrative limit
In vessel T inventory	1 kg	700 g
Global in vessel dust inventory	1 ton	670 kg
Dust on hot surfaces	6 kg of C, 6 kg of W, 6 kg of Be If no C present, 11 kg for Be, and 230 kg for W*	No assessment available

* ITER Organisation has recently (2009) reduced this limit to 77 kg W.

microns of the full tungsten divertor would result in approximately a ton of eroded materials. Safety issues related to this dust include contribution to in-vessel tritium inventory, a radioactive source term in case of accidental release to the environment, potential hydrogen production from reaction with steam in the event of an accidental water leak, and the potential for a dust explosion following hydrogen production and accidental introduction of air.

The tritium used as fuel in tokamak reactors is radioactive and decays to helium-3 by the emission of an electron, also known as beta decay, with an energy of 18.6 keV. Tritium has a half-life of 12.32 years. Surface morphology can affect tritium retention and it has been shown that bubbling can highly affect the retention of hydrogen isotopes [24, 25]. Because of the environmental impact in the case of accidental release, the mobilisable in vessel tritium inventory must be kept as low as reasonably achievable. [26]

1.4 Electrothermal Plasmas

Electrothermal plasma sources using confined capillary arc discharges have previously been used to investigate the erosion of plasma-facing components under disruption-like conditions [27-29]

An electrothermal plasma describes a plasma which is both thermal - where electrons and ions are in thermal equilibrium - and created by electrical discharge. High density ($10^{23} - 10^{27}/m^3$) electrothermal plasmas with temperatures in the range of 1-5eV can be created using a method known as capillary discharge [30-32]. Plasmas created by this method have a wide range of potential applications including space propulsion [33], hypervelocity launchers [34], pellet injection systems for fusion reactors [35,36], and material deposition systems [37].

Of particular note, these plasmas can act as sources of blackbody radiation, allowing for the deposition of high levels of heat flux on a material surface [17,24]. The plasma from electrothermal sources can achieve heat fluxes on the same order as those expected in large tokamak reactors over similar time scales. The sources operate in the ablation controlled arc regime, producing high-density plasmas over 100s of μs with heat fluxes on the order of several GW/m^2.

1.5 Motivation for and Goals of the Study

Although experience through the operation of ITER is expected to allow operation of fusion reactors under non-disruptive conditions, very limited disruptions may still occur. These disruption events will deposit heat fluxes greater than 10GW/m^2 to first wall materials -larger than previously encountered in tokamak reactors. Surface effects on plasma facing materials can lead to serious lifetime issues for components. Clearly, any disruption in future large-scale tokamak reactors could prove catastrophic if it ablates or otherwise causes the migration of a significant amount of material, causes the accumulation of activated material in the vacuum vessel, or creates large amounts of aerosols or dust. Furthermore, a need exists for research on small plasma impact angles. Candidate materials need to be extensively validated against heat fluxes of similar magnitude, time scale, and impact geometry.

The purpose of this work is the study of the erosion of tungsten at small impact angle under heat fluxes and time scales similar to disruption events in future large tokamak reactors. Utilizing the scanning electron microscopy and energy dispersive x-ray spectroscopy techniques the following are investigated:

1. Quantity of material eroded

2. Characteristics of the plasma-exposed surface, including: melt-layer formation and dynamics, splashing of melted material, ejection of solid material, and degredation of the surface through bubble formation or cracking.

3. Characteristics of the ejected material, including evidence of splashing.

Chapter 2

Disruption Simulation

Tungsten possesses a number of favorable qualities for exposure to tokamak plasma. Tungsten has a low sputtering yield and high sputtering threshold energy. At atmospheric pressure, tungsten melts at 3695 Kelvin and boils at 6203 Kelvin. Tungsten has low vapor pressure (1.3×10^{-7} Pa at the melting point) and high thermal conductivity (approximately 150W/mK at room temperature) which does not decrease much with temperature increase. The small time periods experienced during disruption events allow for minimal melting and vaporization of the tungsten. The high energy plasma, however, can degrade tungsten surfaces in the tokamak vacuum vessel by the creation of voids. Additionally, the melted and resolidified tungsten surface has the potential to flake off. A large body of work has been performed on simulating the effects of disruption-like conditions on tungsten.

Figure 2.1: Solid, liquid, and vapor states are typically observed on tungsten during disruption simulation. ([38] Hassanein, A., and I. Konkashbaev. "Lifetime evaluation of plasma-facing materials during a tokamak disruption." Journal of nuclear materials 233 (1996): 713-717. Used under fair use, 2014.)

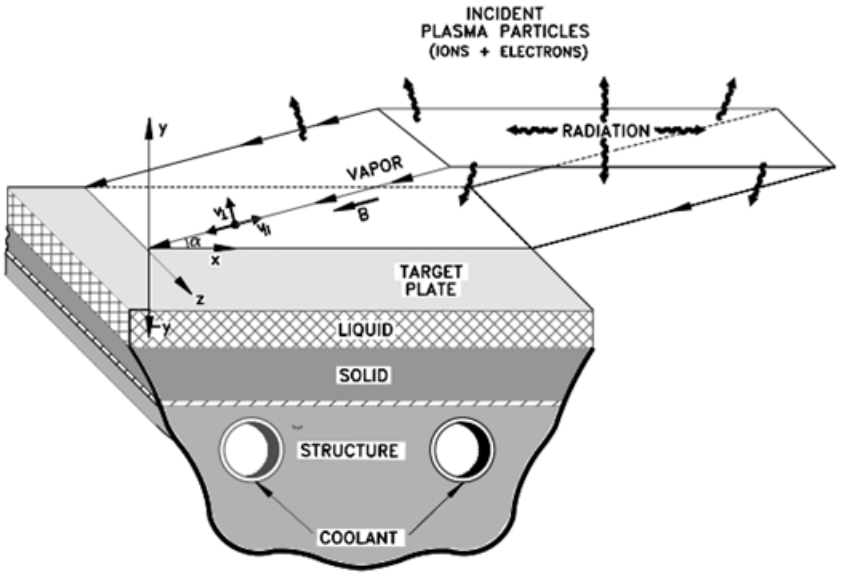

2.1 Observed Surface Effects

When tungsten is exposed to ultra-high heat flux, solid, liquid, and vapor phase layers form. Figure 2.1 shows a diagram of this separation on a tokamak vacuum vessel surface. The layer of melted material will be exposed to a number of forces. These include electromagnetism, mechanical vibration, plasma momentum, plasma pressure, surface tension, ablation recoil, and gravity. In metal plasma facing components, a large portion of erosion lifetime is expected to be determined by the evolution and hydrodynamics of the melt layer during off-normal events. Additionally, the dominant forces which act on a melt layer will determine

Figure 2.2: Illustration of the vapor shielding effect. ([39] Gilligan, J., D. Hahn, and R. Mohanti. "Vapor shielding of surfaces subjected to high heat fluxes during a plasma disruption." Journal of Nuclear Materials 162 (1989). Used under fair use, 2014.)

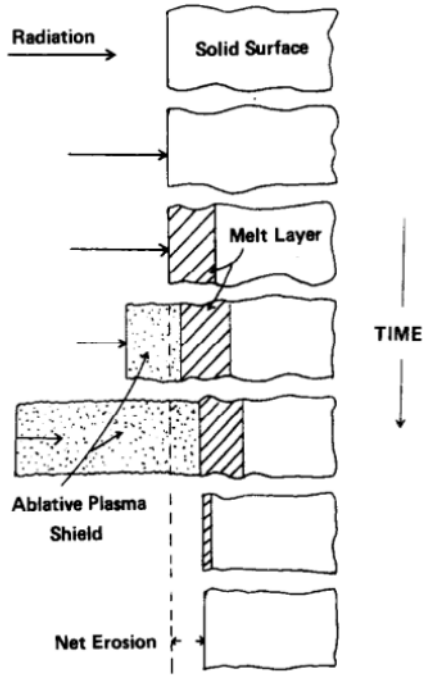

the surface structure upon resolidification. Two factors which affect amount of material melt and ablation are vapor shielding and the fluid dynamics of the melt-layer.

The vaporization of matter from a surface results in a vapor cloud or shield. Material ablation due to high heat flux is inhibited by vapor shielding.[39-41] A digram demonstrating the mechanism is shown in Figure 2.2. Immediately following initial ablation, the ablated surface material "absorbs" incoming radiation, reducing the total energy transported to the ablating surface. Higher energy ions will be able to penetrate the vapor shield more than low energy ions - resulting in a higher vapor shielding effect for low-energy plasmas.

Figure 2.3: Time evolution of simulated plasma-liquid volume fraction fields of tungsten during instability. ([43] Miloshevsky, G., and Ahmed Hassanein. "Modeling of macroscopic melt layer splashing during plasma instabilities." Journal of Nuclear Materials 415.1 (2011): S74-S77. Used under fair use, 2014.)

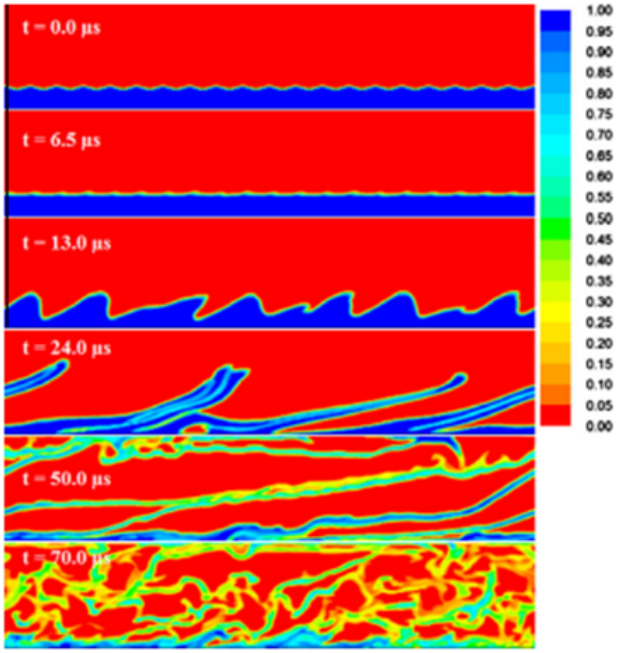

Fluid instabilities can occur in melt layers on material surfaces. Two major types of instabilities are hypothesized to occur under disruption-like conditions: Kelvin-Helmholtz instabilities and Raleigh-Taylor instabilities [42]. Raleigh-Taylor instabilities are thought to develop at locations where the normal components of the forces at play during disruption events act on the liquid surface. Kelvin-Helmholtz instabilities can develop from high velocity shears caused by plasma wind.

Significant losses can occur from instabilities in the melt-layer [43]. Figure 2.3 shows a

Figure 2.4: Simulated ablation loss and melt-layer thickness for small-angle impact at 10 GW/m^2. ([44] Hassanein, A., and I. Konkashbaev. "Comprehensive physical models and simulation package for plasma/material interactions during plasma instabilities." Journal of nuclear materials 273.3 (1999): 326-333. Used under fair use, 2014.)

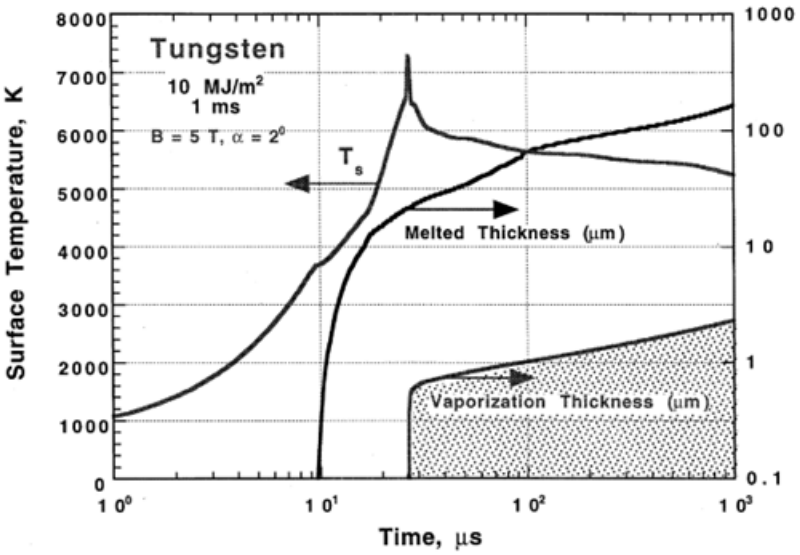

simulation of tungsten plasma-liquid interface modeled with the software package FLUENT. The figure demonstrates flow of two incompressible plasma-liquid tungsten fluids separated by a sharp interface and subject to gravity, surface tension, and disturbed by a surface wavelength. In the figure, blue represents liquid-phase and red represents plasma-phase. When the liquid layer is subjected to perturbation by plasma streams of approximately 10^7 cm/s, surface disturbances develop on the liquid surface. When long (2mm) waves form on the liquid surface, 80-90% of the melt layer is lost in macroscopic liquid ligaments.

Figure 2.4 shows selected results of the A*THERMAL-S code which is used to study

surface erosion due to vaporization along with other disruptive effects [44]. The results shown give the time evolution of surface temperature, melt-layer thickness, and vaporization losses of tungsten for a disruption with incident plasma energy of $10MJ/m^2$ over 1 ms at an incident angle of 2 degrees. The sharp decrease in surface temperature is due to a vapor shielding effect. In general, vaporization losses on plasma facing surfaces during short plasma instabilities are found to be small compared to the thickness of the melt-layer. On metallic components, the thickness of the melt layer can be up to two orders of magnitude higher than the vaporized thickness.

2.1.1 Void/Bubble Formation

Helium bombardment has been shown to lead to bubbling/void formation in tungsten. Figure 2.5 shows SEM images of tungsten substrates which have been exposed to helium plasmas of various energies in the divertor plasma simulator, NAGDIS-II [45]. The NAGDIS-II device exposes materials to helium plasmas with ion fluences of 1-4 x $10^{23}/m^2$. The top row shows the material surface while the bottom shows a cross section. Tungsten substrates were continuously exposed to helium plasma for a period of two hours and with energies from 1-30 eV. The authors conclude that bubbles form under the specific conditions that the He ion energy is greater than 5eV and the tungsten surface temperature exceeds 1600K. The energy limit corresponds to energy required to overcome the surface barrier potential energy of solid tungsten. The temperature limit is necessary for generation of thermal vacancies in solid tungsten.

Figure 2.5: Bubble size and generation in solid tungsten is highly dependent on incident ion energy. ([45]Nishijima, Dai, et al. "Formation mechanism of bubbles and holes on tungsten surface with low-energy and high-flux helium plasma irradiation in NAGDIS-II."Journal of nuclear materials 329 (2004): 1029-1033. Used under fair use, 2014.)

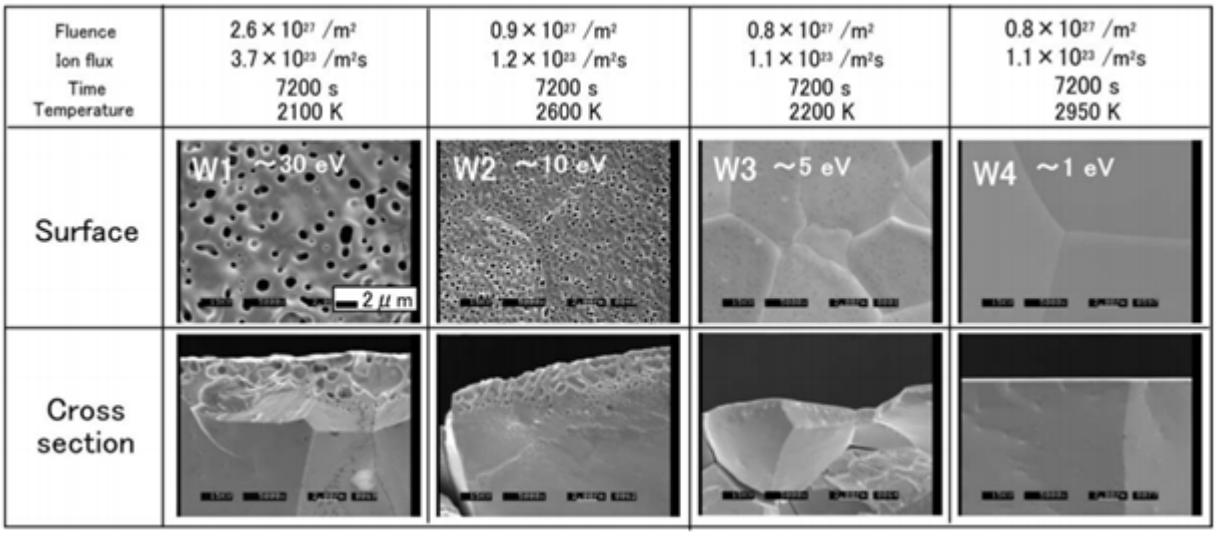

Figure 2.6: Cross sectional view of bubbles/voids observed in resolidified tungsten samples which have been exposed to plasma in TEXTOR. ([46] Coenen, J. W., et al. "Tungsten melt layer motion and splashing on castellated tungsten surfaces at the tokamak TEXTOR." Journal of Nuclear Materials 415.1 (2011): S78-S82. Used under fair use, 2014.)

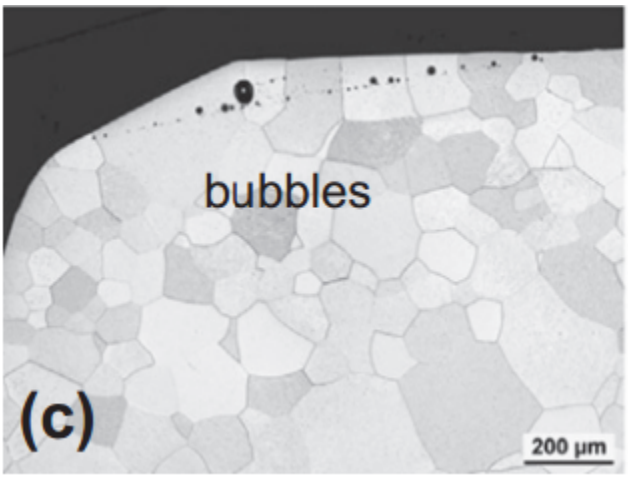

Bubbles/voids formed under melt conditions have been observed in the German-based tokamak TEXTOR [46]. In this work, tungsten plates were exposed to tokamak plasma for 2-4 seconds at 35 degrees, allowing a total heat flux of 45MW/m^2. Figure 2.6 shows an SEM cross section of an area of tungsten which has melted and resolidified after being exposed to the tokamak plasma. Bubble/void size ranges from the order of microns to the order of tens of microns. The authors attribute the formation of these voids to shrinkage cavitation - cavities which form to accommodate the density difference between solid and liquid upon rapid solidification.

Figure 2.7: Relationship between surface temperature and ion energy on bubble/void formation in tungsten. ([48]Kajita, Shin, et al. "Formation process of tungsten nanostructure by the exposure to helium plasma under fusion relevant plasma conditions." Nuclear Fusion 49.9 (2009): 095005. Used under fair use, 2014.)

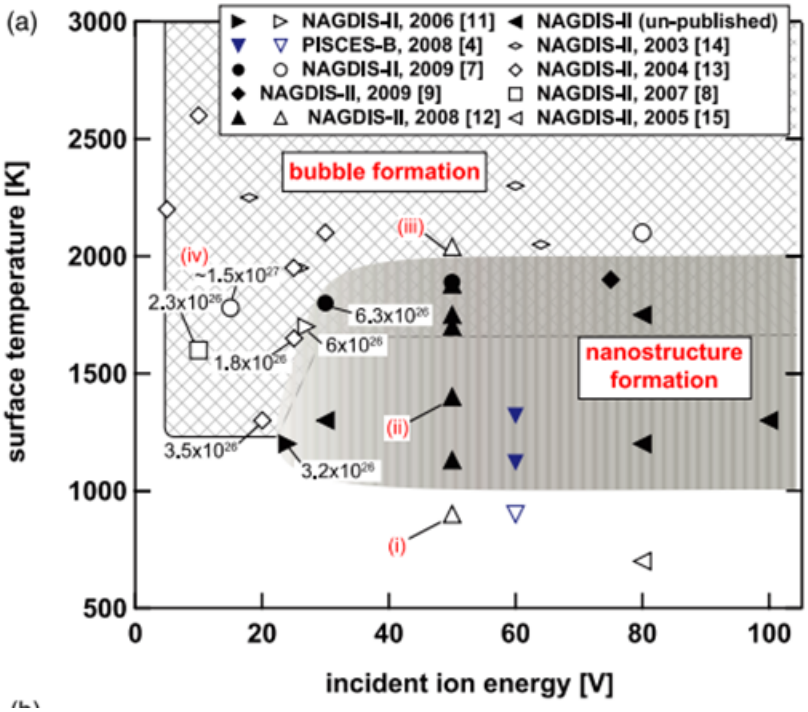

2.1.2 Emergent Nanostructure

Surface temperature and incident ion energy have been shown in the NAGDIS I and II experiments to play a large role in the observed morphology of tungsten exposed to disruption-like conditions [47]. Long periods of plasma exposure have shown development of nanostructured surface elements. Figure 2.7 shows results of the NAGDIS-II divertor simulator. Filled markers represent instances where nanostructure formation is observed. When surface tem-

Figure 2.8: Long periods of He plasma exposure have been shown to lead to the development of nanostructures on tungsten surfaces. ([48]Kajita, Shin, et al. "Formation process of tungsten nanostructure by the exposure to helium plasma under fusion relevant plasma conditions." Nuclear Fusion 49.9 (2009): 095005. Used under fair use, 2014.)

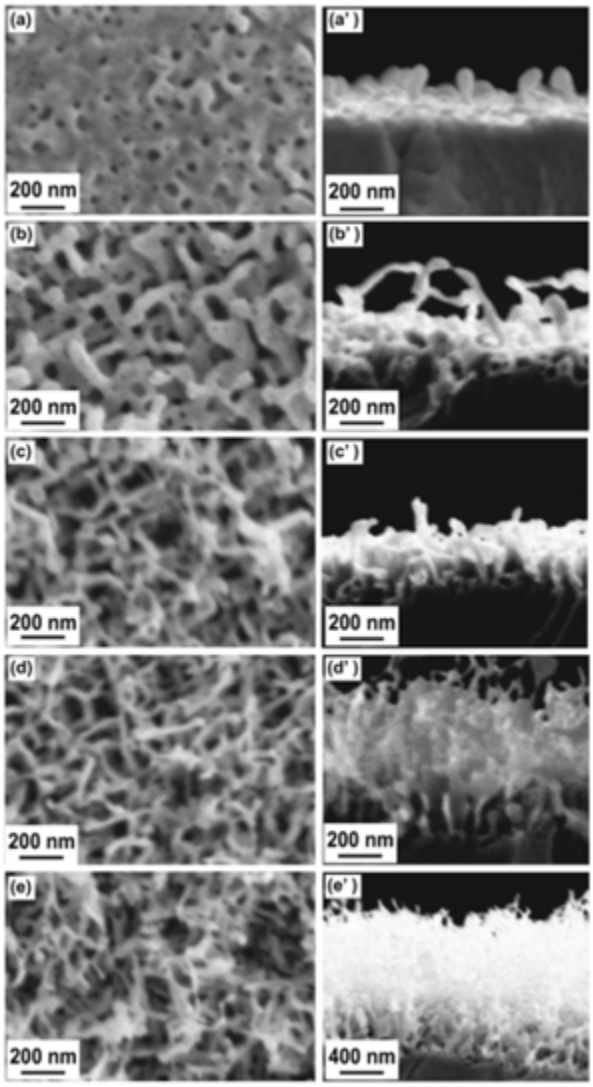

perature is in the range of 1000-2000K and the incident ion energy is greater than 20eV, nanostructure formation occurs. At energies less than 20eV, or surface temperatures greater than 2000K, many holes are observed on the tungsten surface. No nanostructure is observed under these conditions.

Figure 2.8 shows SEM images of tungsten substrates exposed to helium plasmas for various time periods in the divertor plasma simulator, NAGDIS-I [48]. The NAGDIS-I device exposes materials to helium plasmas with ion fluences of 1-3 x $10^{25}/m^2$. The samples were polished to a mirror finish before being exposed to helium plasma for 375s, 700s, 1125s, 1500s, and 3400s. Surface temperature of the samples were measured to peak at around 1400 Kelvin. In figure 2.7(a) bubbles and pinholes less than 100nm in diameter were observed. At longer exposure times, (b)-(e) a the surface evolved in fiber-like nanoscale structures.

2.1.3 Splashing

Melt-layer splashing occurs when liquid-phase drops are ejected from a material surface and can lead to significant erosion [49-51]. Two main mechanisms have been shown to lead to splashing effects and are illustrated in figure 2.9. One path is considered to occur from Kelvin-Helmholtz instabilities. Melt flow can lead to ejection of material from a surface when the inertia of the liquid overcomes surface tension. The second mechanism which can lead to splashing is the formation of vapor bubbles within a melt layer. In addition to incident particles dissolving in the liquid, bubbles can form as a result of continuous heating

Figure 2.9: Splashing caused by instability (left) and bubble formation (right). ([52] Hassanein, Ahmed, A. Konkashbaev, and I. Konkashbaev. "Erosion of melt layers developed during a plasma disruption." Presented at the 18th European Symposium on Fusion Technology, Karlsruhe, Germany, 22-26 Aug. 1994. Vol. 1. 1994. Used under fair use, 2014.)

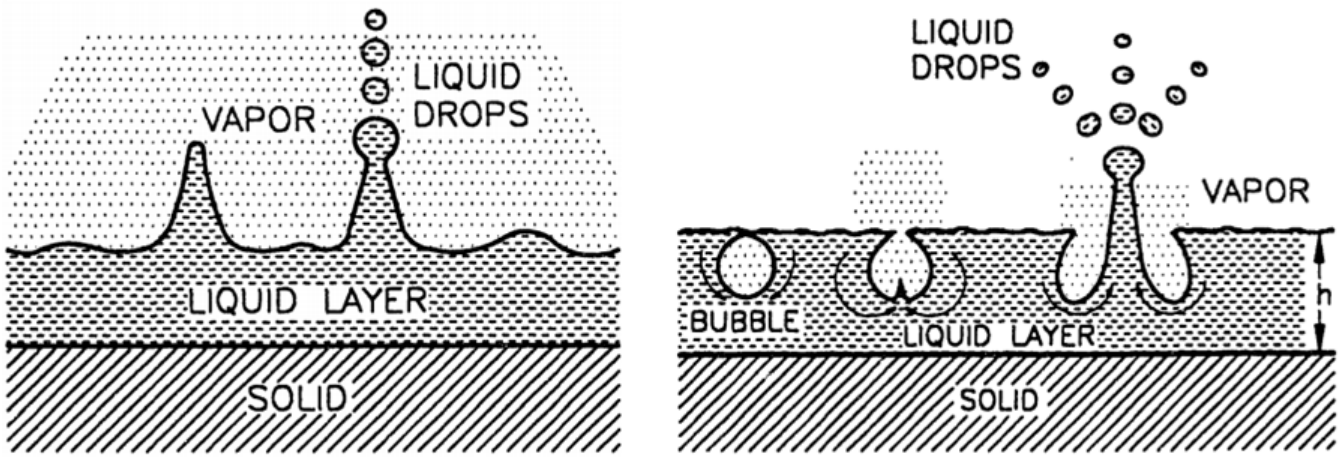

and overheating of a liquid layer during plasma exposure. During this exposure, the surface temperature of the liquid layer can exceed the equilibrium vaporization temperature. The overheating will cause the growth of bubbles. As these bubbles appear at the liquid/plasma interface they rapidly expand and explode, ejecting portions of the melt layer. The amount of material ejected and size of droplets will depend on a large number of parameters including the material properties, plasma parameters, and degree of overheating.

Figure 2.10 shows splashing observed in the QSPA facility. This facility is further detailed in the next section. Tungsten samples were placed 60cm from a plasma gun at normal incidence. The pulse duration is between 0.4 and 0.6 ms and exposes the material

Figure 2.10: Significant splashing observed at the QSPA facility. ([50] Klimov, N., et al. "Experimental study of PFCs erosion under ITER-like transient loads at plasma gun facility QSPA." Journal of Nuclear Materials 390 (2009): 721-726. Used under fair use, 2014.)

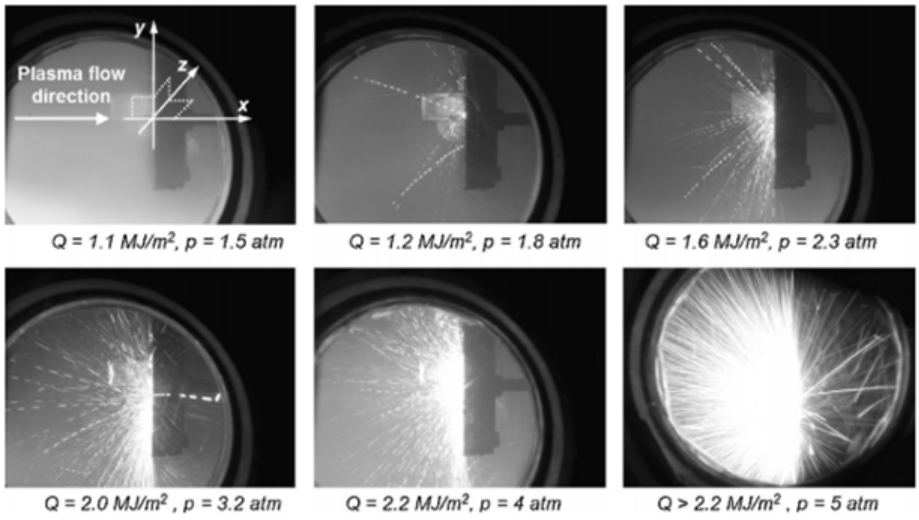

surface to 0.8-5.5GW/m^2.

Figure 2.11 shows similar splashing observed at the German-based tokamak, TEXTOR [46]. Tungsten plates were placed in the path of electron and ion drift, exposing the surface to approximately 20MW/m^2 at 35 degrees with respect to the magnetic field over a period of 2-4s. The researchers note two distinct phenomena - a fine spray of small droplets on the order of microns and more random larger drops on the order of 1-20 microns with an average drop size of 4 microns. Figure 2.12 shows a histogram giving size distribution of tungsten drops redeposited on the plate. Drop size is most frequently 3-4 microns.

Figure 2.11: Spraying (left) and splashing (right) of tungsten observed in experiments performed at the TEXTOR tokamak. ([46] Coenen, J. W., et al. "Tungsten melt layer motion and splashing on castellated tungsten surfaces at the tokamak TEXTOR." Journal of Nuclear Materials 415.1 (2011): S78-S82. Used under fair use, 2014.)

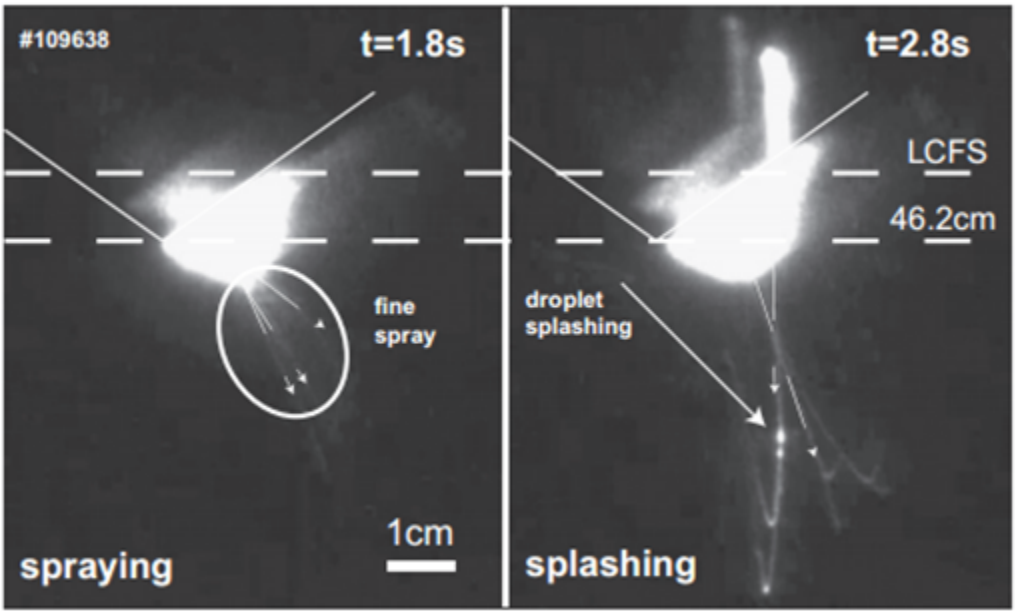

Figure 2.12: Tungsten splash drop redeposition sizes from experiments performed at the TEXTOR tokamak. ([46] Coenen, J. W., et al. "Tungsten melt layer motion and splashing on castellated tungsten surfaces at the tokamak TEXTOR." Journal of Nuclear Materials 415.1 (2011): S78-S82. Used under fair use, 2014.)

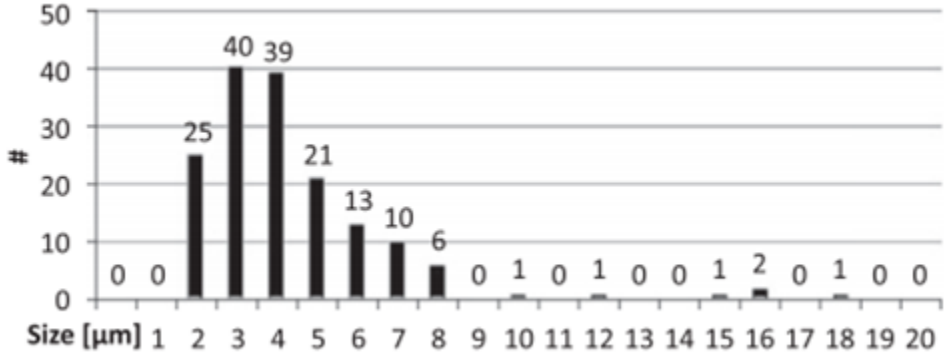

2.2 Electrothermal Plasmas as Sources of High Heat Flux

Thermal loads on the order of what is expected to be relevant to ITER are not achieved in existing tokamaks. Therefore, other devices such as ion sources [53], electron beams [54, 55], and plasma guns [50, 56] are used in the testing of PFCs.

2.2.1 The MK-200 UG Device

A diagram of the MK-200 UG facility is shown in figure 2.13 [56]. The device consists of a pulsed plasma gun, a long drift tube, and a target chamber. A 1152μF capacitor bank

Figure 2.13: The MK-200 UG device generates and compresses a plasma along a drift tube before sample exposure. ([56] Arkhipov, N. I., et al. "Material erosion and erosion products in disruption simulation experiments at the MK-200 UG facility." Fusion engineering and design 49 (2000): 151-156. Used under fair use, 2014.)

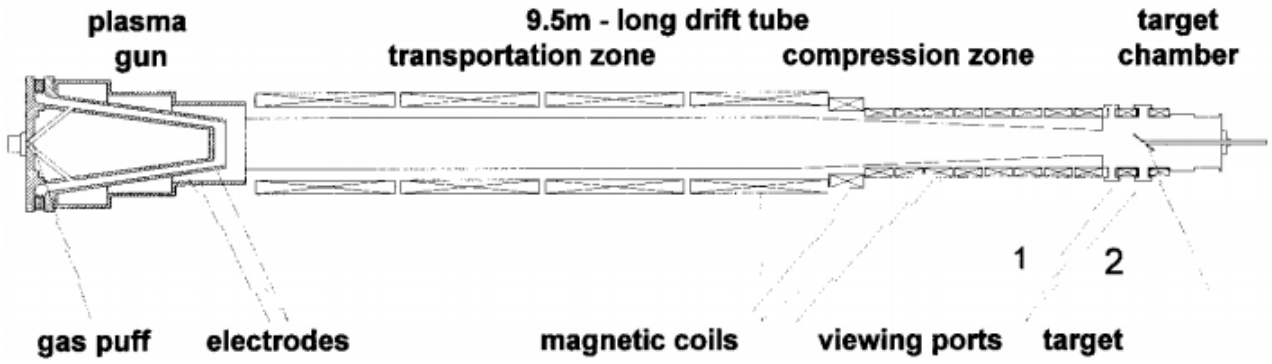

supplies the device with 25kV, corresponding to 360kJ of stored energy. The drift tube is a 6.5m cylider followed by 3m cone which reduces the diameter from 30cm to 15cm. A magnetic field ranging from 0.7T to 2.5T confines the plasma as it travels down the tube.

The exiting hydrogen plasma stream has a power density of 300-400 GW/m^2 and a number density of up to 2 x $10^{22}/m^3$. The ion energy is 1.5keV and the pulse duration is 40-50 μs. Samples placed in the vacuum chamber are exposed to plasma which exits the drift tube and can be arranged such that the plasma impact occurs at any incidence.

Figure 2.14 shows a tungsten sample exposed to hydrogen plasma generated by the MK-200 UG device. A fine mesh of intergranular cracks cover the material surface. The researchers conclude there is no evidence of melt-layer motion or fluid instability. The same

Figure 2.14: Normal impact from the MK-200 UG device showing the microstructure of a tungsten surface exposed to the plasma stream. ([56] Arkhipov, N. I., et al. "Material erosion and erosion products in disruption simulation experiments at the MK-200 UG facility." Fusion engineering and design 49 (2000): 151-156. Used under fair use, 2014.)

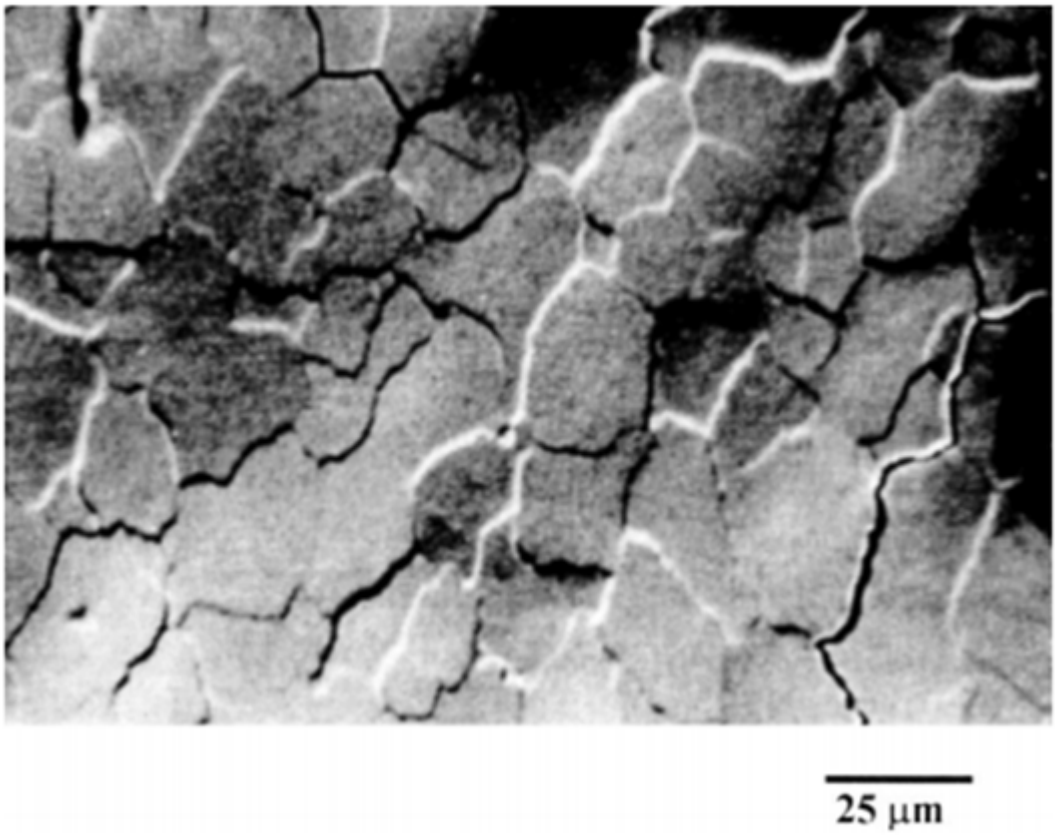

Figure 2.15: The QSPA device exposes samples to flow directly from a plasma gun. ([50] Klimov, N., et al. "Experimental study of PFCs erosion under ITER-like transient loads at plasma gun facility QSPA." Journal of Nuclear Materials 390 (2009): 721-726. Used under fair use, 2014.)

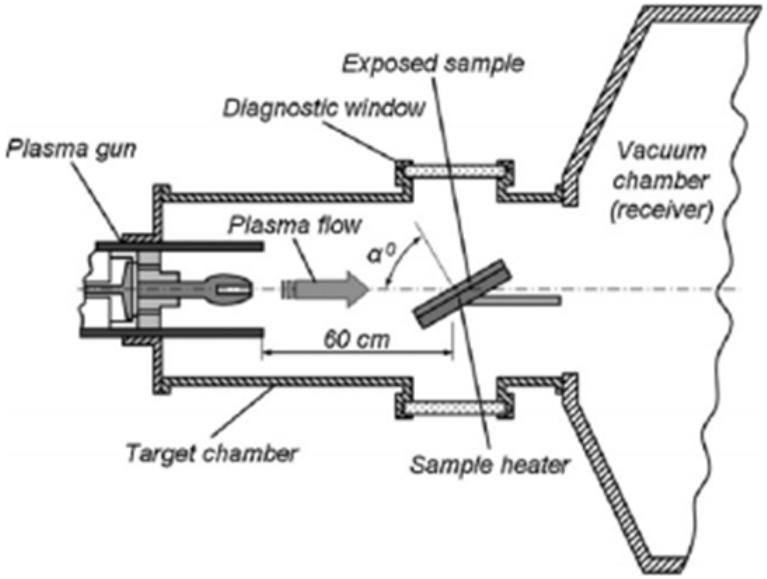

experiment found splashing of liquid tungsten drops from the material surface of 1-200μm in diameter.

2.2.2 The QSPA Device

Figure 2.15 gives a schematic of the QSPA device [28, 50]. A series of capacitors provide a plasma gun with 2-3.7kV. The hydrogen plasma exits the gun and travels down the length of a target chamber. This plasma then impacts the sample which can be placed at any incidence. The impacting plasma has an energy density which ranges from 8.3-300GW/m^2 over 0.4-0.6

ms. Ion energy has a range from 100-600 eV. Plasma density ranges from $10^{22} - 10^{23}/m^3$

A tungsten sample irradiated by the QSPA device is shown in figure 2.16. Although there is no large evidence of surface flow, a melt layer several microns thick can be observed in the sample cross section. A network of micro- and major cracks have developed across the material surface. The major cracks extend deep (400 microns) into the bulk material.

Figure 2.16: The QSPA decive has been used to show evidence of surface melting and cracks which propagate deep into the material. ([28] Garkusha, I. E., et al. "Performance of deformed tungsten under ELM-like plasma exposures in QSPA Kh-50." Journal of Nuclear Materials 415.1 (2011): S65-S69. Used under fair use, 2014.)

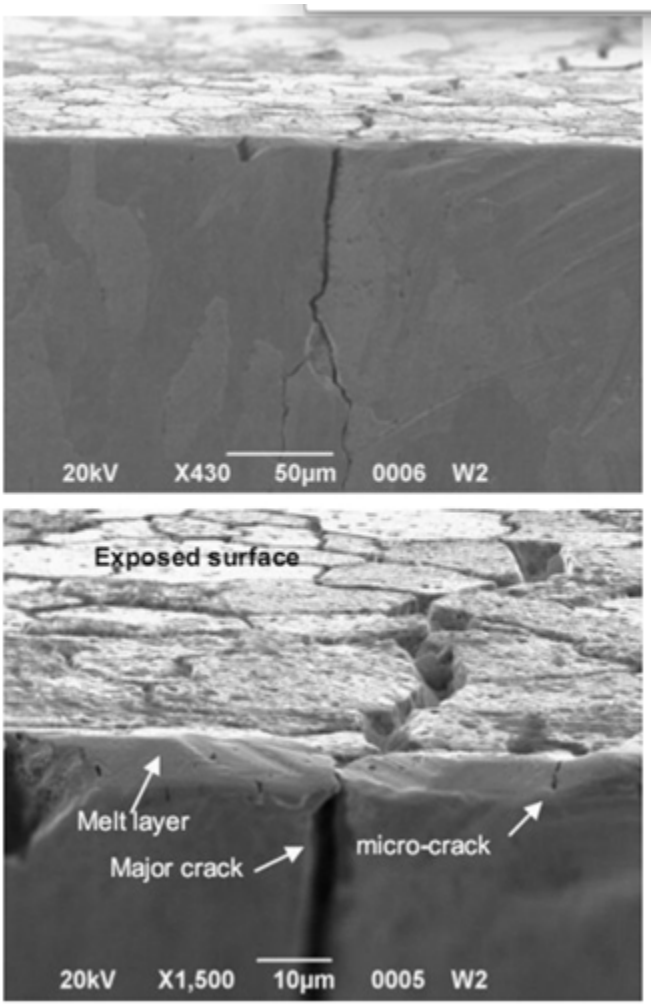

Chapter 3

Experimental Setup

3.1 The Plasma Interaction with Propellant Experiment, PIPE

In this work, the Plasma Interaction with Propellant Experiment (PIPE) has been used study the surface behavior of tungsten under disruption-like conditions. PIPE is composed of a grounded outer cylindrical electrode, an insulator that houses the ablating capillary sleeve, and an inner electrode. Figure 3.1 shows a schematic of an electrothermal plasma source and Figure 3.2 shows the PIPE apparatus.

When discharged, the energy radiated to the walls of the capillary is absorbed by the interior surface, which causes direct ablation of the liner material to a dense vapor without passing through a liquid state. The ablated material is then ionized to form a plasma which

Figure 3.1: Schematic of an electrothermal capillary discharge source.

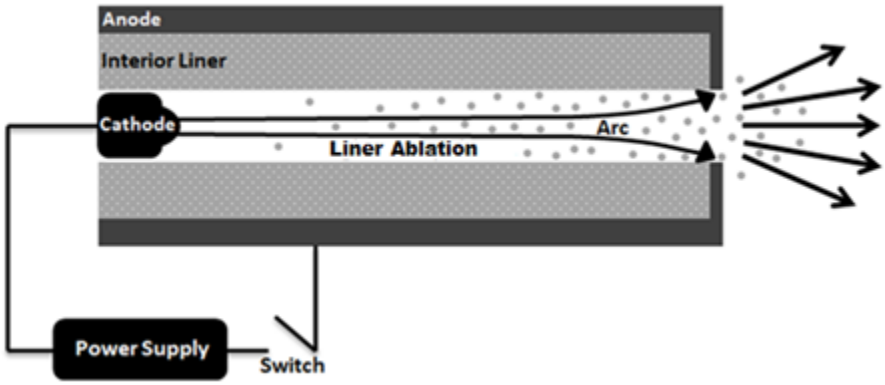

Figure 3.2: The disassembled (left) and assembled (right) PIPE apparatus.

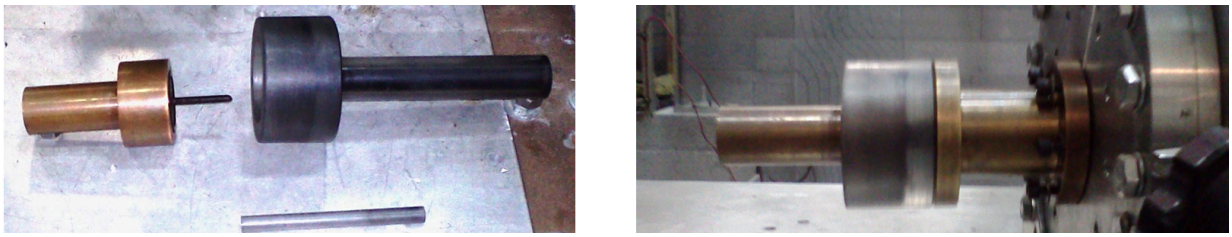

Figure 3.3: Illustration of high heat flux ablation

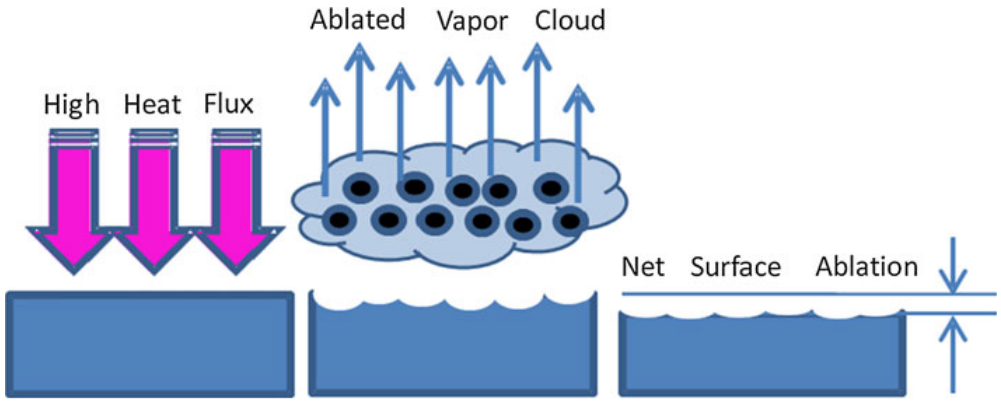

acts as a blackbody radiation source, providing a high heat flux to exposed surfaces [30,32]. This process is illustrated in Fig 3.3. The relevance of ET plasma as a simulator for hard disruption induced erosion is in its ability to deposit radiative heat flux on the inner wall of a replaceable liner material thereby producing ablation similar to the hard disruption conditions found in tokomaks.

As the plasma temperature increases during a discharge, the plasma resistance drops. This in turn allows more plasma to pass through the channel. More material is ablated as current increases, increasing the plasma number density and kinetic pressure within the capillary. This cycle continues until no more joule heating occurs. The capillary in PIPE is 9cm long and 4mm in diameter, giving it an aspect ratio, capillary radius to capillary length R/L, of 0.022. Because of this small aspect ratio, the plasma parameters can be taken to be constant over the capillary cross section [41, 57, 58]. The PIPE device produces plasmas with energy ranging from 1-3 eV over hundreds of microseconds. This corresponds to a plasma

Figure 3.4: Measured current of a PIPE discharge.

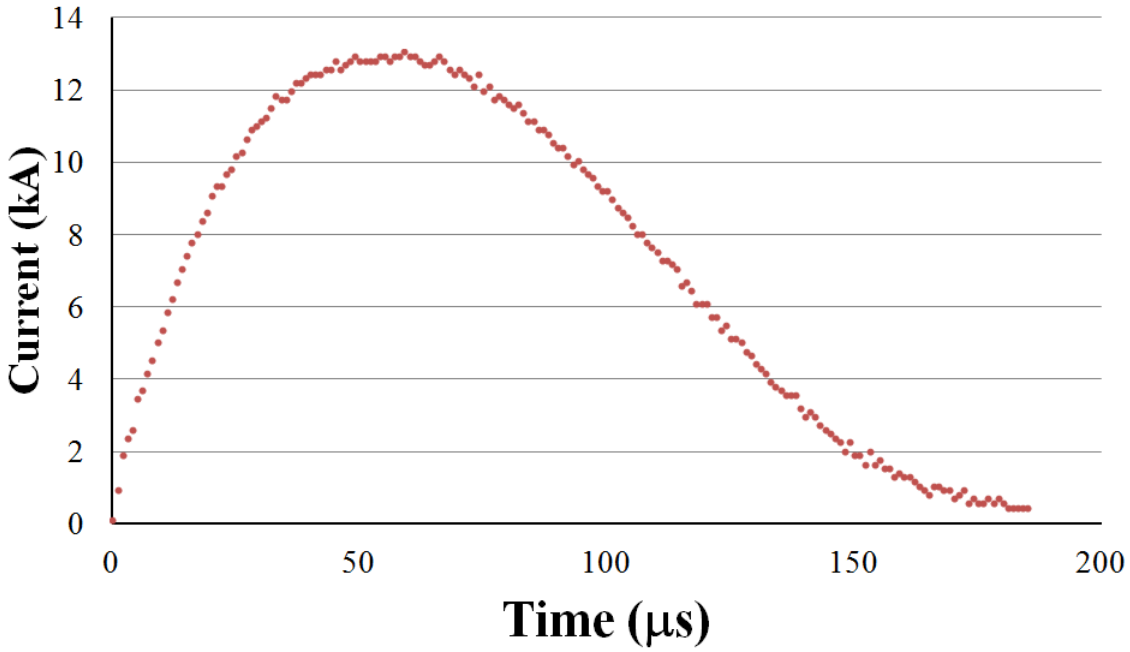

temperature of 10,000-35,000 Kelvin. Heat fluxes produced in the PIPE device are on the order of 10-100GW/m^2 and plasma pressures can exceed 100MPa. Voltage is measured by a compensated capacitively coupled high voltage probe and discharge current by a Pearson coil. A sample discharge current is shown in Figure 3.3.

The work presented in this thesis has been investigation on the ablation and melting of tungsten and Lexan liner materials in the PIPE experiment under disruptive conditions. Figure 3.4 shows the experimental setup for these discharges.

Sleeves of tungsten and Lexan were machined and outfitted to the experiment. For the tungsten discharge, insulating Lexan endcaps were placed on either side of the experimental sleeve. Another insulating Lexan sleeve was placed between these materials and the conduct-

Figure 3.5: Experimental setup of PIPE for this work

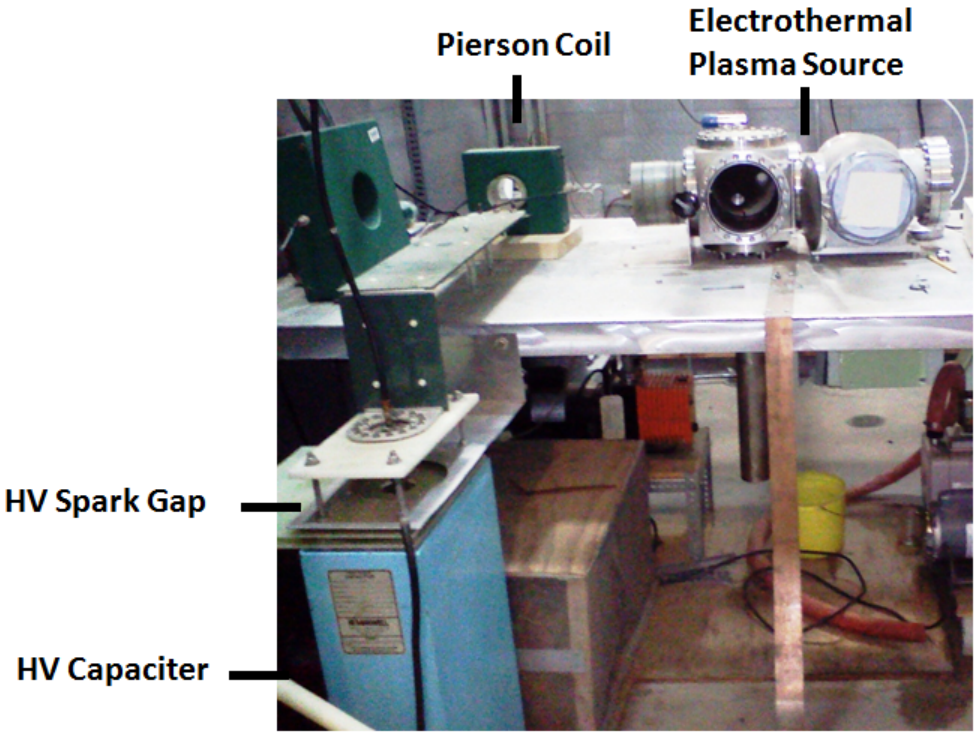

Figure 3.6: Dimensions of tungsten sleeve and Lexan endcaps.

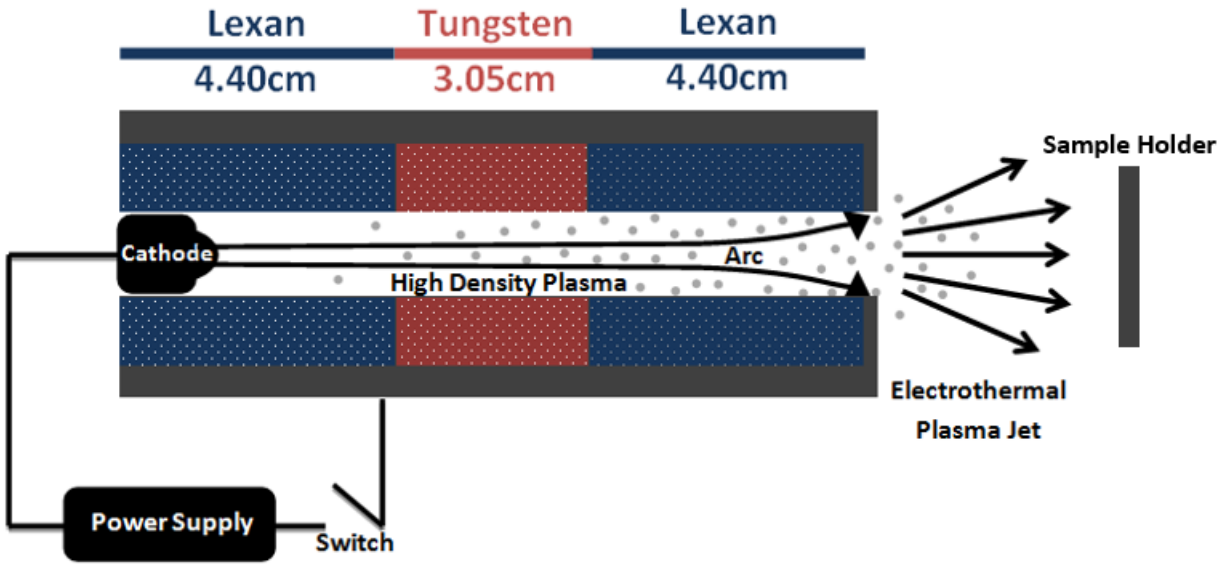

Figure 3.7: Dimensions of full Lexan sleeve.

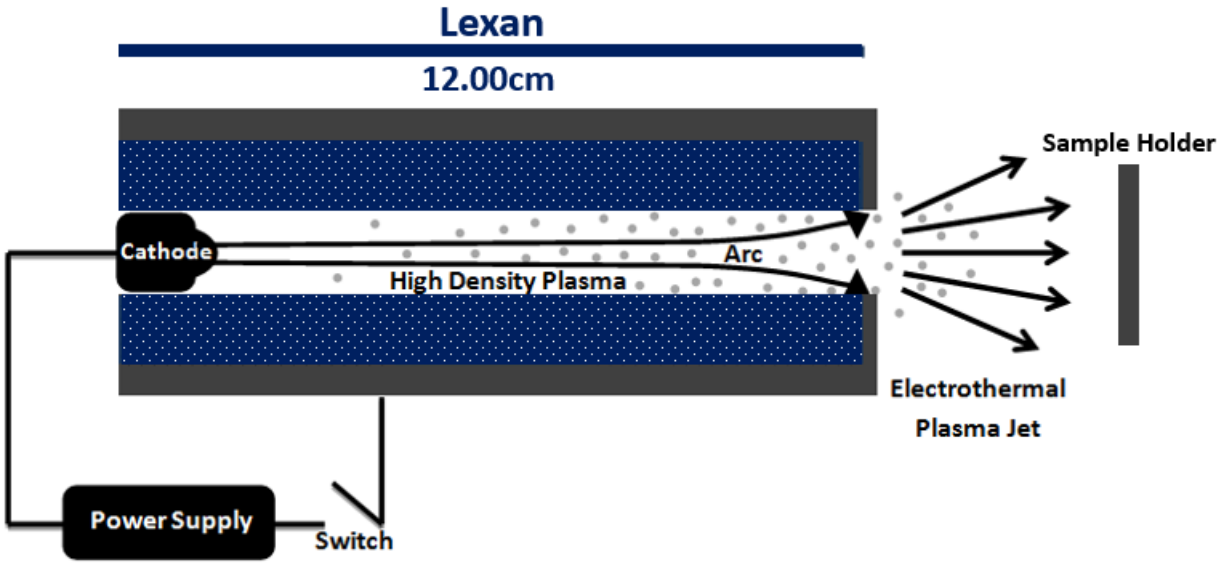

ing anode. This second sleeve forces the discharge arc to travel the length of the capillary instead of through a conductive experimental sleeve. Figure 3.5 shows the dimensions of the metal and lexan endcaps. In the tungsten discharge the sleeve consists of 4.40cm lexan, 3.05cm tungsten, and 4.40cm lexan. A second sleeve was machined consisting only of Lexan so that the effects of a discharge on Lexan could be observed. Figure 3.6 shows a diagram of this sleeve.

Material loss was determined by weighing the sleeve materials and the outer lexan sleeve prior to and following discharge. To perform cross-sectional analysis, the tungsten sleeve was cut using a low-speed saw with a diamond blade, then polished with silicon-carbide polishing paper and alumina suspension to 0.02 micron grit.

3.2 Scanning Electron Microscopy

Scanning Electron Microscopy (SEM) is a variety of electron microscopy that scans a surface with a focused beam of electrons to produce images. The SEM provides two large benefits over optical microscopes: it extends resolution limits to the nanometer range and improves depth-of-focus resolution by a factor of almost 300 [59].

Figure 3.7 shows a diagram of a SEM microscope. The basic components of an SEM microscope include the electron source, optics, and detector systems. The electron source generates electrons and accelerates them to between 0.1 and 40kV. The generated beam passes through a series of lenses which reduce the beam spot size. This beam spot size is a limiting factor in the resolution of images produced SEM. The beam then interacts with the sample surface, producing two classes of electrons known as secondary electrons and backscatter electrons. These electrons are then picked up by detectors. The electron beam scans across a surface to produce an image.

The electron beam interacts with a sample surface in a number of ways. Figure 3.8 shows a generalized diagram describing these interactions. Secondary electrons are emitted within the first nanometers of a surface. These electrons are generated when beam electrons inelastically interact with k-shell electrons of the sample. The low energy of these electrons (less than 50eV) only allows for detection from the first nanometers of a material surface. Because surfaces closer to the detector will give higher electron counts, topography is the main contrast mechanism when imaging secondary electrons.

Figure 3.8: General diagram of a scanning electron microscope. ([60] Wittke, James. "Instrumentation." Northern Arizona University, 2008. http://www4.nau.edu/microanalysis/Microprobe-SEM/Instrumentation.html. Used under fair use, 2014.)

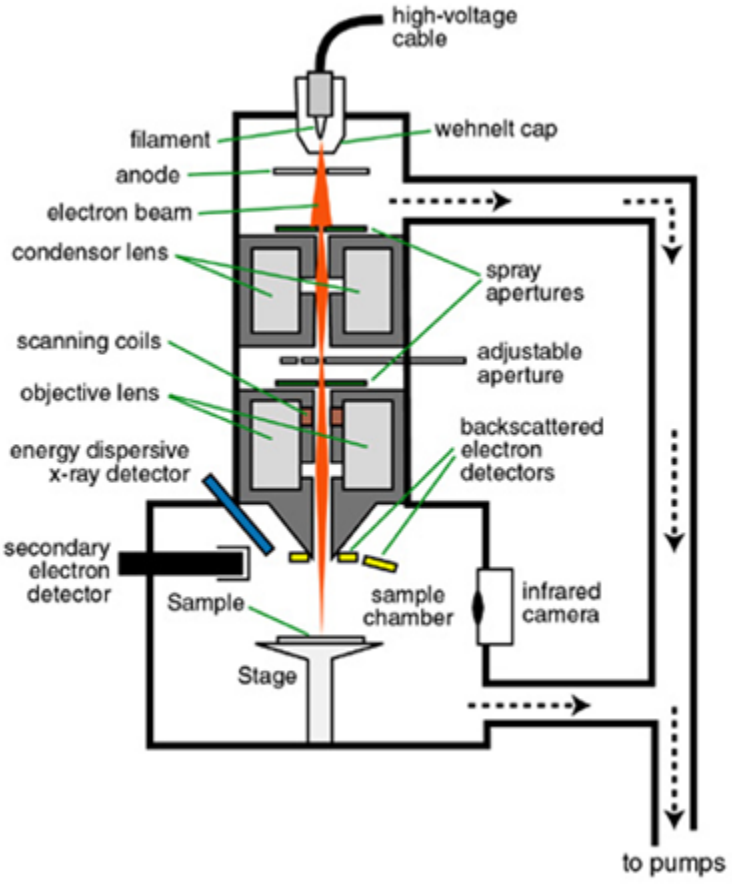

Figure 3.9: Interaction volume of SEM electrons and general location of produced electrons and x-rays. ([60] Wittke, James. "Instrumentation." Northern Arizona University, 2008. http://www4.nau.edu/microanalysis/Microprobe-SEM/Instrumentation.html. Used under fair use, 2014.)

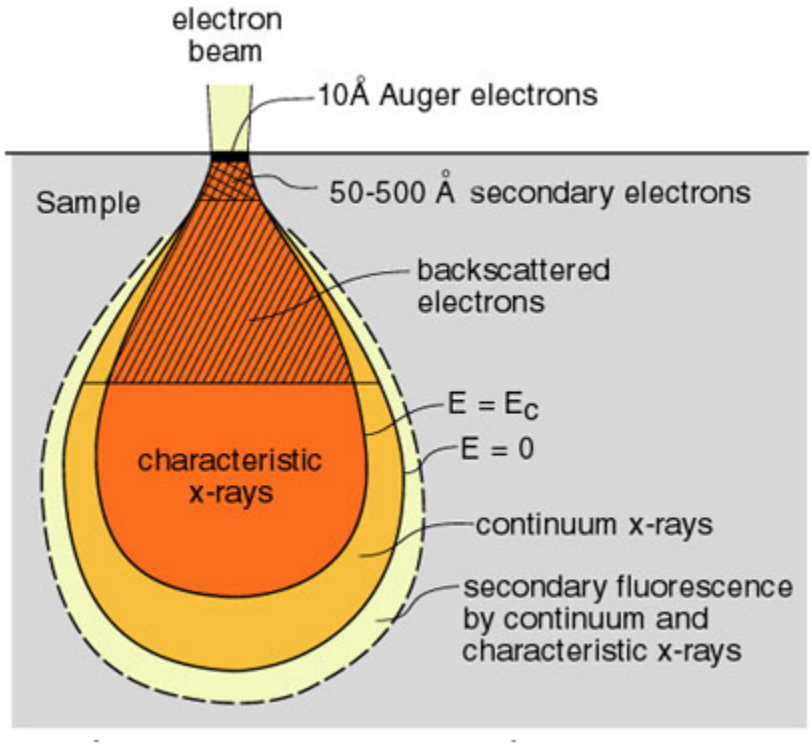

The second variety of imaged electrons, backscattered electrons, are beam electrons which are reflected or backscattered by out of the sample by elastic interactions. The contrast mechanism for backscattered electrons is composition. Because heavy elements backscatter electrons more strongly than light elements, high-Z elements will give a greater signal and appear lighter.

Because SEM samples are imaged with electron beam, charge can build up on the material surface if the sample cannot conduct away the charge. A common solution to this problem is to coat nonconductive samples with an ultrathin layer of conductive material. An additional advantage of coating is improved signal/noise ratio for low-Z samples. This effect is a result of the higher secondary electron emission for high-Z materials which are typically used in coatings.

3.2.1 Energy Dispersive X-ray Spectroscopy

Energy Dispersive X-ray Spectroscopy (EDS) is a method by which a SEM equipped with an x-ray detector can measure the near-surface elemental composition of a sample. When an inner-shell electron is ejected from an atom by the incident electron beam, an electron from another shell can fill the vacancy. In doing so, an x-ray of an energy characteristic to the element can emitted to account for the energy difference between the two orbitals.

As figure 3.9 illustrates, x-rays are emitted from the bulk of the sample, not the surface. Exact penetration depth is a function of the material and energy of the electron beam. Higher

energy beams will penetrate further into the bulk than lower ones and higher-Z materials will have less penetration than low-z materials. The dimensions of the penetration volume are on the order of tenths of microns to a few microns. EDS is sensitive to around 1000 ppm. EDS can be accurate to about 2% (weight %) without standards. Greater accuracies can be achieved with clean, flat samples, long x-ray collection times, and the use of standards.

Chapter 4

Results

Work has been performed on the ablation of physical liner material in the PIPE experiment under disruptive conditions. The 3450μF high-voltage capacitor was charged to 3.30kV for discharges over tungsten with lexan and pure lexan. The tungsten discharge had a residual voltage of 1.33kV - leaving the discharge voltage as 1.97kV. The lexan sleeve experienced discharge under similar conditions. The tungsten and lexan sleeves were both weighed prior to and following discharge. For the tungsten/lexan discharge the difference in weight of the tungsten was a loss of 58.4mg. Assuming uniform ablation, this corresponds to 4.0μm across the full tungsten sleeve.

Figure 4.1: Tungsten sleeve at 500x magnification.

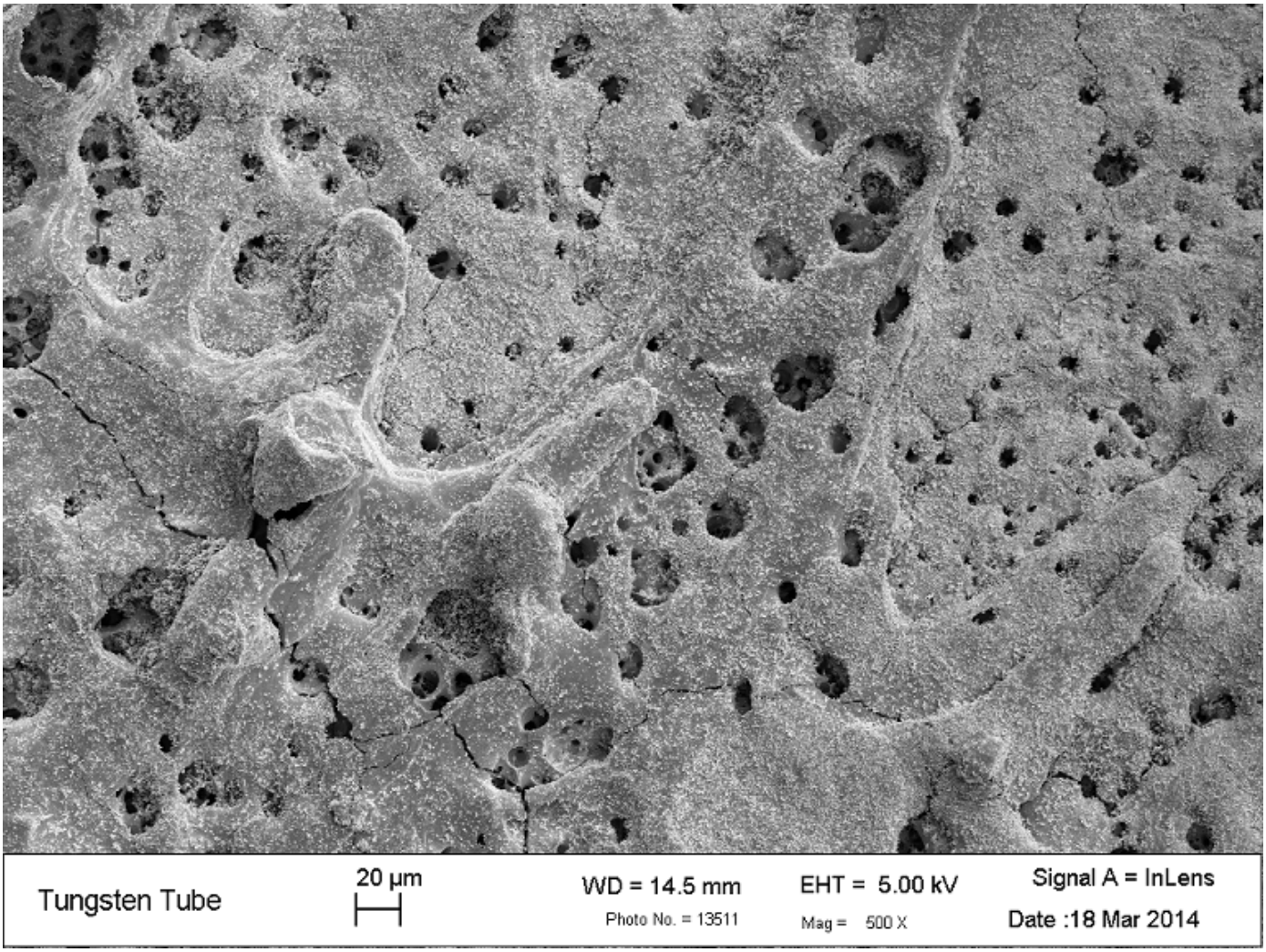

Figure 4.2: Tungsten sleeve at 2000x magnification.

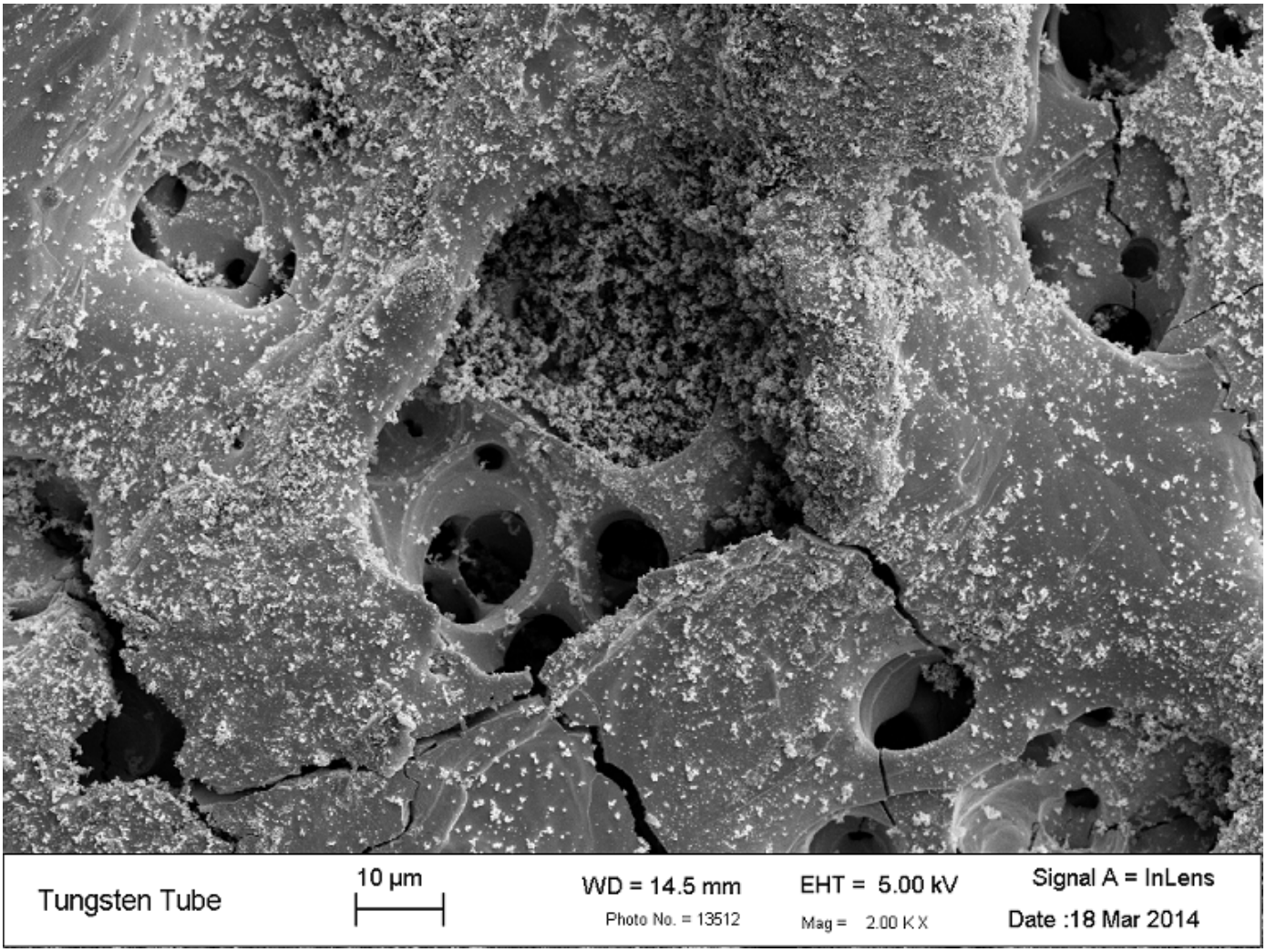

4.1 The Tungsten Sleeve

Figures 4.1, and 4.2 show SEM images of the post-shot tungsten sleeve at 500x magnification and 2000x magnification respectively. A number of features are observed on the material surface. Melt-layer flow is evident in figure 4.1. Voids exist on the post-exposure material surface. Void diameter is on the order of 2-20 microns in diameter. Cracking is also observed on the material surface.

The melt flow is observed to travel down the tube length and is likely dominated by plasma wind effects. Observed cracking is likely the effect of rapid cooling.

A SEM image of the sample cross-section is shown in figure 4.3. The voids observed on the tungsten surface are seen to extend around 20 microns into the material bulk. Additionally, at the depth of 20 microns an interface exists between light and dark regions of tungsten. EDS maps taken in this region do not show significant difference in composition between the light and dark regions. It is possible that a reduction in material hardness caused by plasma exposure allow tungsten within the first 20 microns to be abraded more readily than bulk tungsten. Alternatively, the alumina suspension used in the polishing process could have an etching effect which is preferential on the melted/resolidified tungsten. Either of these processes would lead to a difference in height between the affected and non-affected regions and cause the affected region to appear darker in SEM images.

There are a number of mechanisms which could explain the bubble/void formations observed. One explanation of this phenomenon is that the melt-layer of tungsten becomes

Figure 4.3: Cross-section of tungsten sleeve at 3000x magnification.

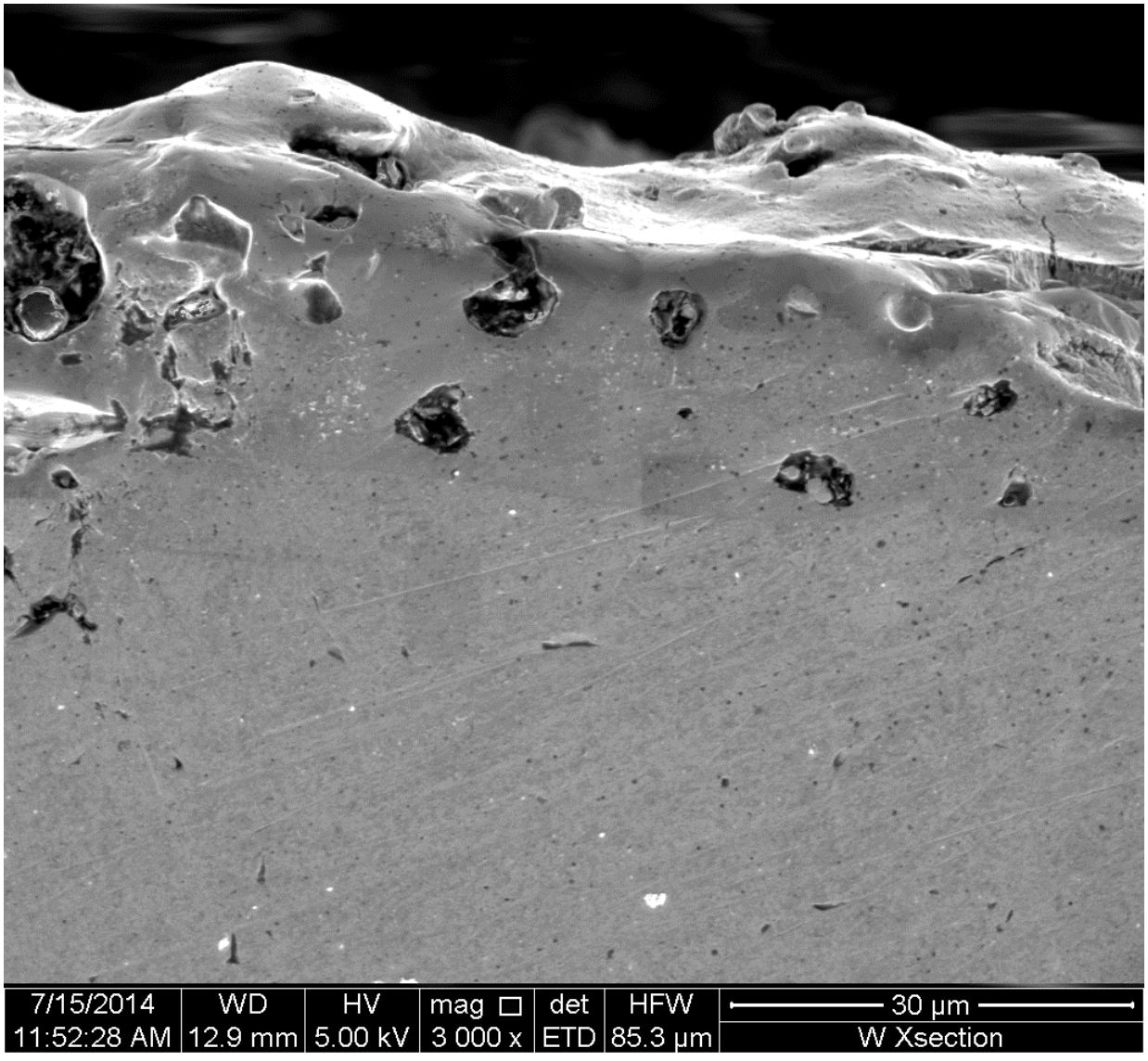

superheated and begins to boil. When the melt-layer rapidly cools, the voids occupied by gaseous tungsten remain. This is an unlikely scenario. The heat transfer in the PIPE device is much more likely to resemble film boiling - where a vapor shield prevents rapid evaporation - than nucleate boiling - where bubbles form in the bulk of a liquid.

Shrinkage cavitivation has been used to explain the presence of similar bubbles in other work. In this process, a rapidly solidifying liquid forms cavities. These cavities are generally dendritic in geometry, however, and are an unlikely mechanism in this scenario.

Finally, it is possible that plasma impact on the material surface leads to the dissolution of gasses, primarily oxygen and carbon dissociated from the ablated lexan, in the molten tungsten. Because the solubility of gas in the molten metal is much greater than the solubility in the solid state, the resolidification of the tungsten forces these gasses out of solution, forming the observed voids.

Figure 4.4 shows a comparison of the melt and ablation results from this work and simulations at similar parameters performed by Hassanein et al [44]. Experimental values are represented on the graph by purple and green circles - vaporization and melt respectively. The simulation and experiment both occur at small angle impact with heat fluxes of approximately 10 GW/m^2. The simulation differs from the experiment in that the simulation occurs under a magnetic field of 2 Tesla and with higher incident ion energy than experiment. This experimental work shows greater vaporization and less melting than is predicted by the model. This difference is likely largely related to the difference in incident ion energy as there will be significantly more vapor-shielding in the lower-energy experimental work. This

Figure 4.4: Comparison of melt and vaporization in PIPE to similar simulations performed by Hassanein et al.

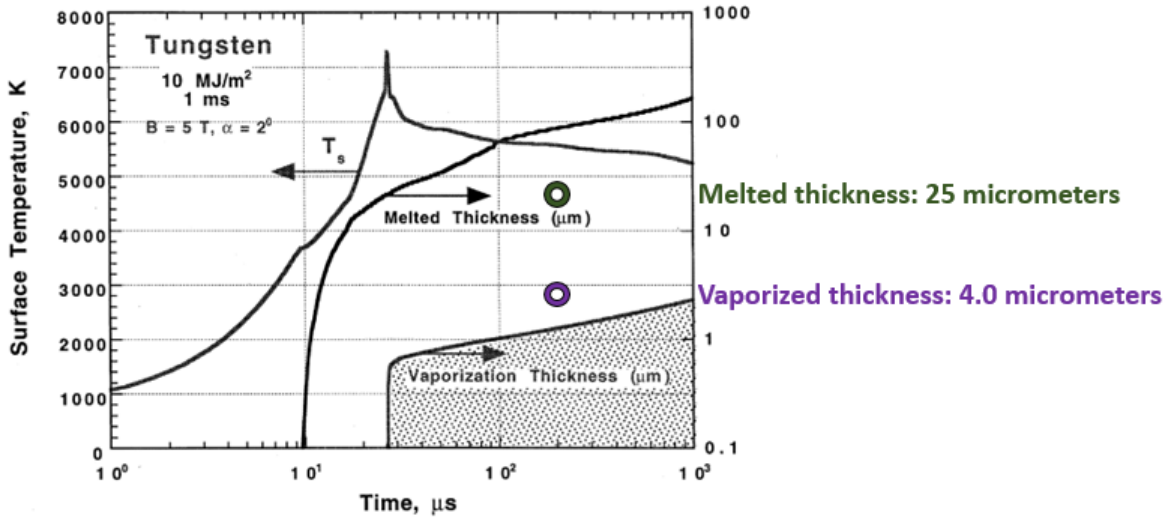

in turn will inhibit the formation of the melt-layer. It is also likely that the melt layer in PIPE is subject to more fluid instability than was simulated in the work of Hassanein et al.

4.2 Ejected Material

Figures 4.5, and 4.6 show SEM images of material ejected from the tungsten/Lexan PIPE discharge at 69x and 500x magnification respectively. Evidence of large-scale flow radiating out from the center of the impact site can be seen in figure 4.5. Surface structures on the order of 5-20 microns can be seen in figure 4.6. There are no observed sites of single-drop impact and solidification of liquid material.

For comparison, figures 4.7 and 4.8 show similar sites of material ejected from the pure

Lexan PIPE discharge at 66x and 500x magnification. Figure 4.7 shows evidence of large-scale flow radiating from impact center and figure 4.8 shows surface structures similar to those seen in the tungsten/Lexan discharge.

EDS analysis has been performed on the ejected material. An example analysis can be seen in figure 4.9. Table 4.1 shows the distribution of elements within the edges of the apparent flow pattern and outside of it. The presence of copper is due to ablation from the device anode. Although the material surface will likely contain a small amount of carbon contamination, carbon and oxygen detected will primarily be seen from the Lexan sleeves. Titanium counts come from the substrate the ejected material was collected on. It is observed that significantly more tungsten exists within the main deposition than outside of it. This would suggest that the flow edge represents tungsten motion.

EDS performed on structures which have the potential to be solid ejected material show these structures to have larger percentages of carbon and oxygen than the general composition and significantly less tungsten. In no case was the tungsten content greater than 15%. This would suggest these structures to be ejected pieces of Lexan. This is consistent with other work on the PIPE device which observes Lexan particulates being ejected during discharge.

No obvious redeposition splatter is observed on the collection plate. Figure 4.10 shows an example of such a splatter in a previous PIPE experiment involving discharge over molybdenum. Because of the similarities in flow seen in both discharges, it is likely that the ablated Lexan is the cause of observed flow-like patterns. Additionally, because there is no z-contrast

Figure 4.5: Material ejected from tungsten/Lexan discharge at 69x magnification.

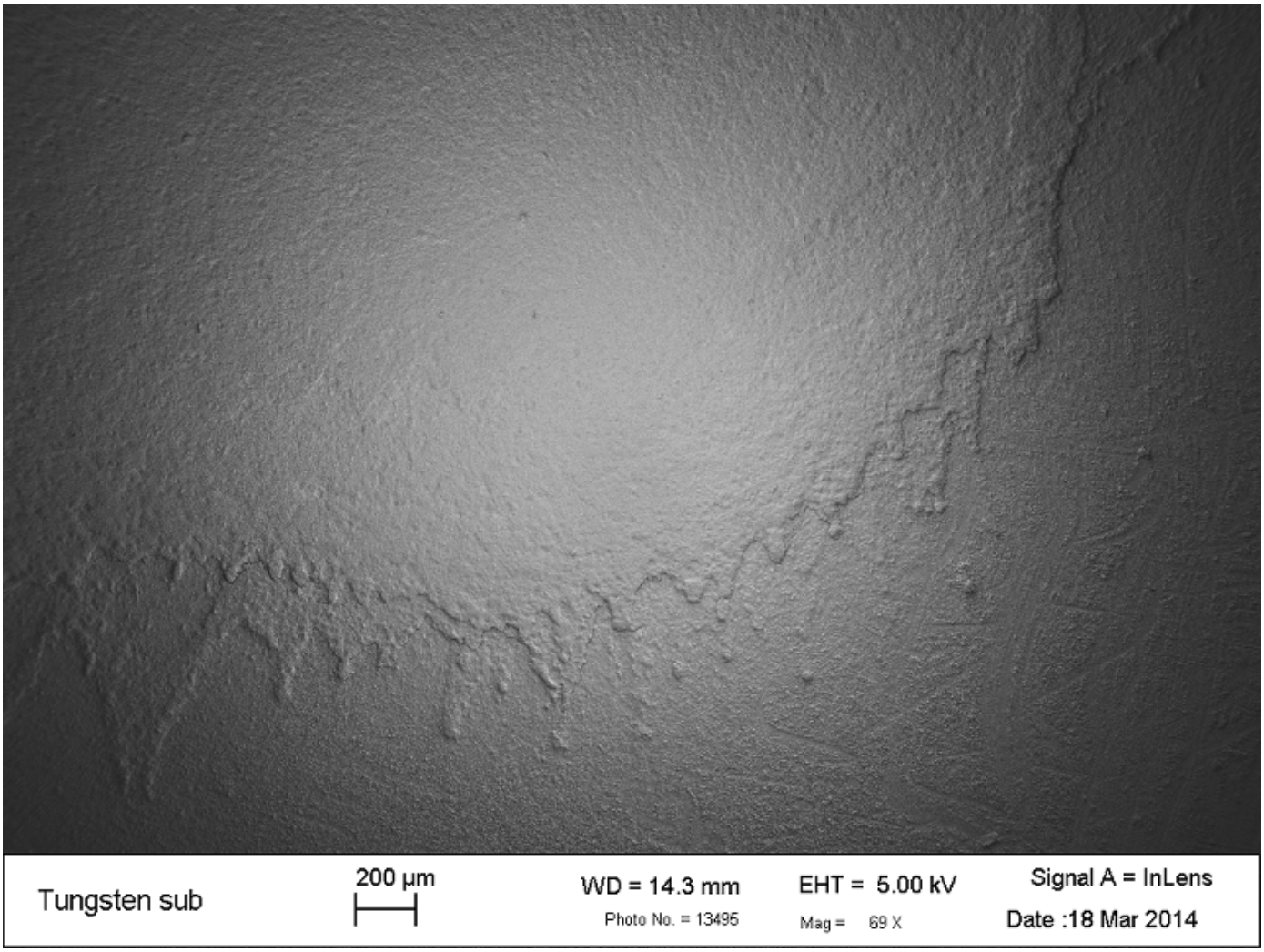

Figure 4.6: Material ejected from tungsten/Lexan discharge at 500x magnification.

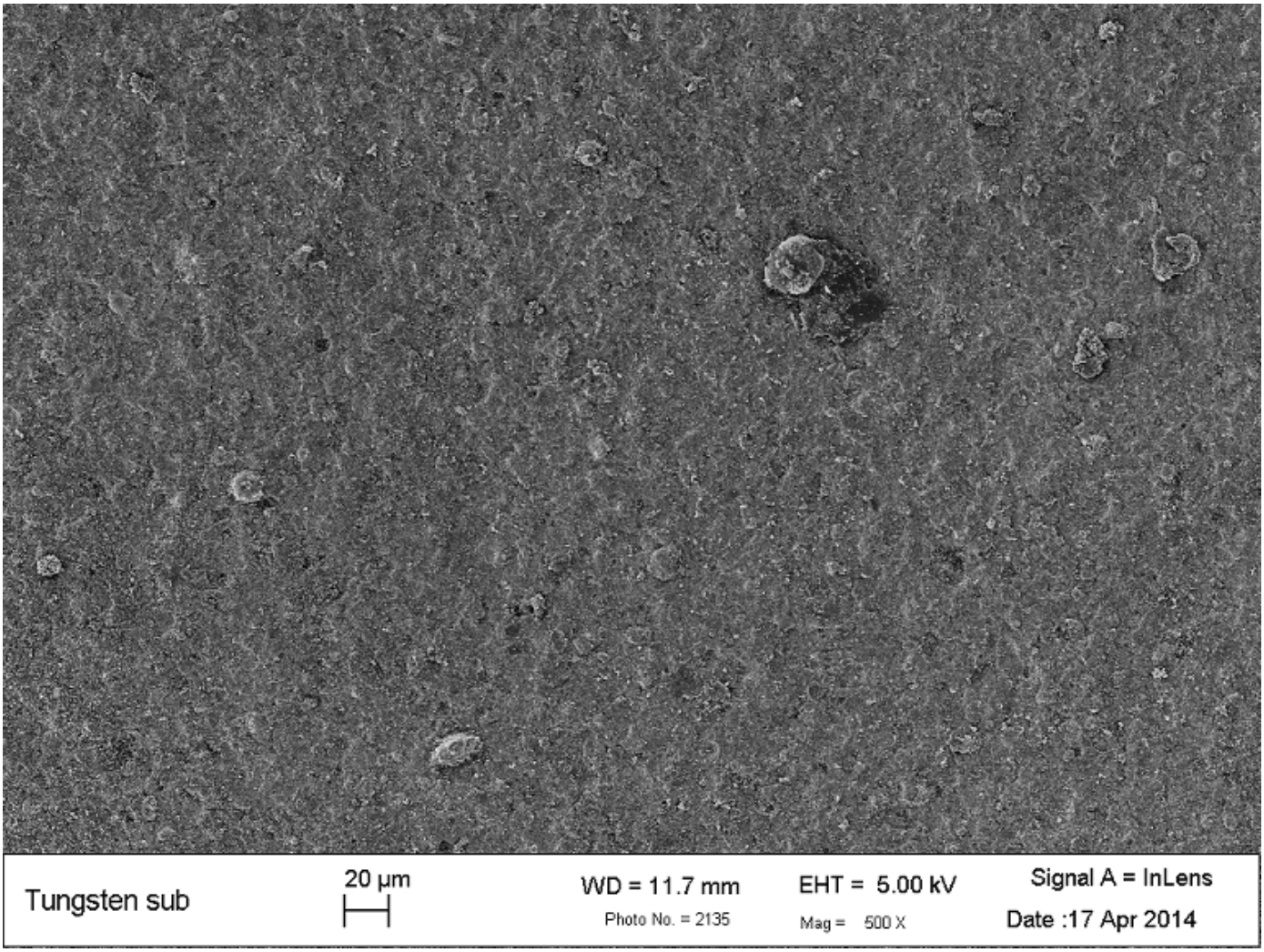

Figure 4.7: Ejected material from pure Lexan discharge at 66x magnification.

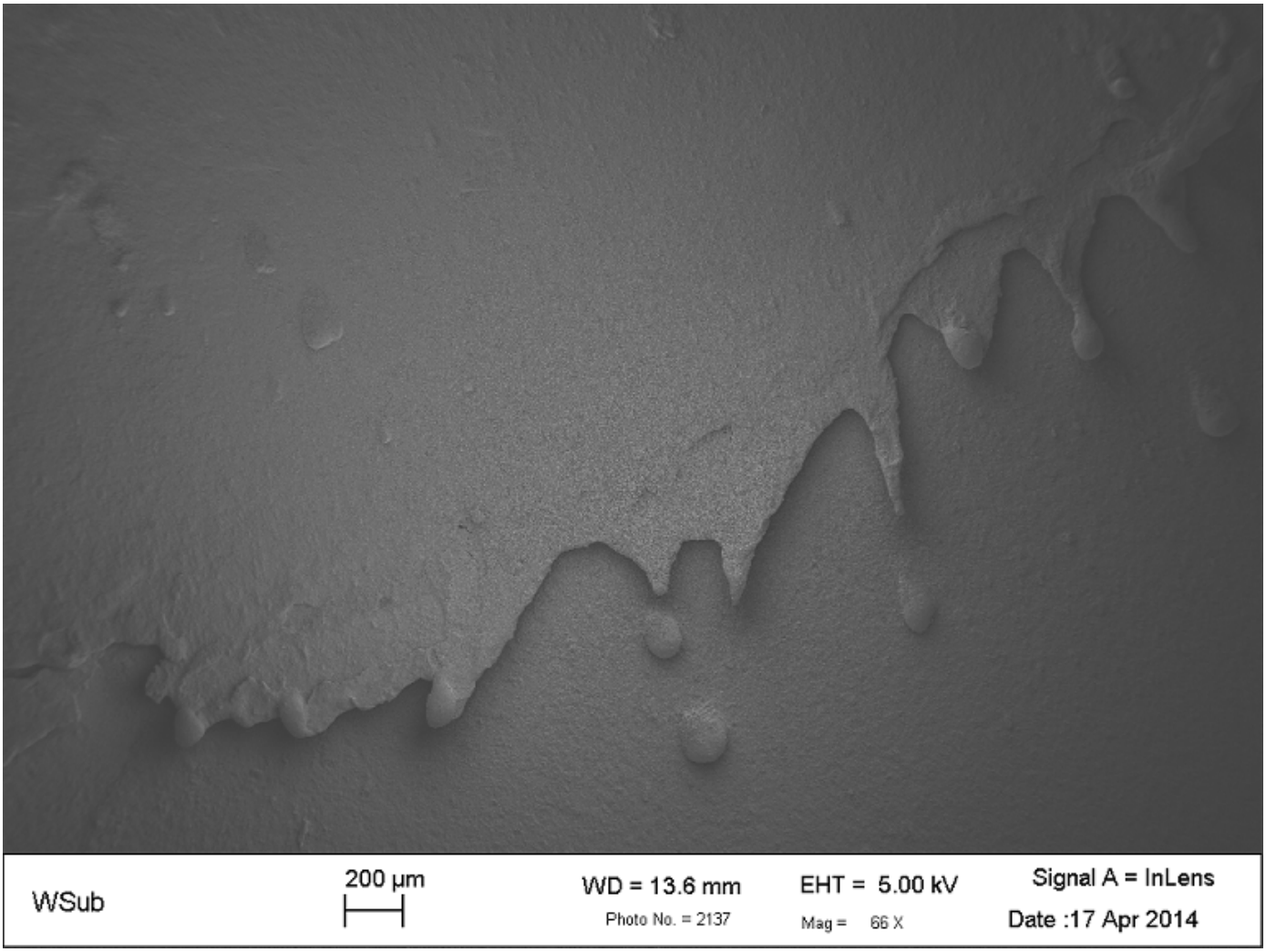

Figure 4.8: Ejected material from pure Lexan discharge at 500x magnification.

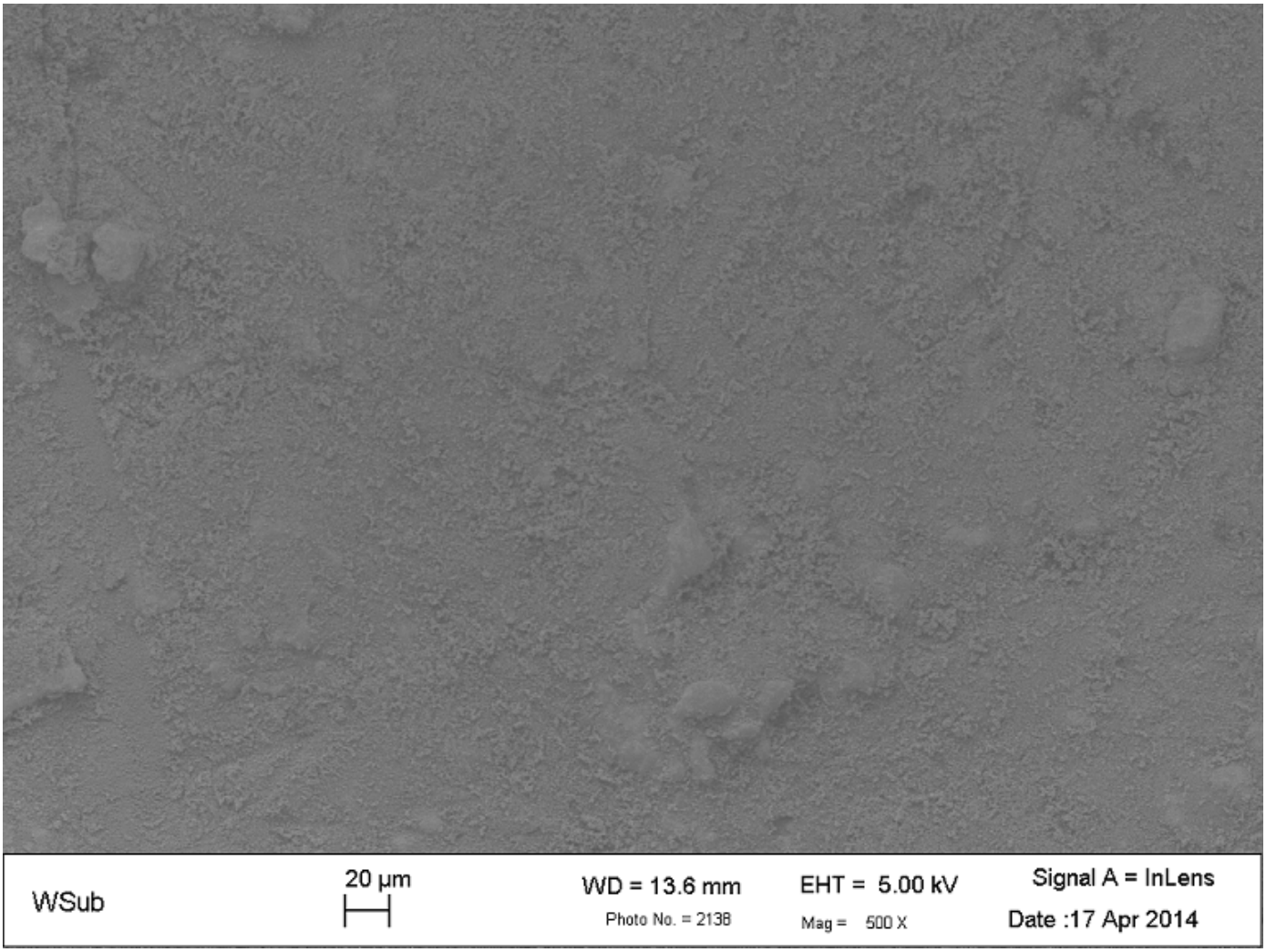

Figure 4.9: Sample EDS analysis showing composition of an approximately 20 micron structure observed in the material ejected from the tungsten/Lexan discharge.

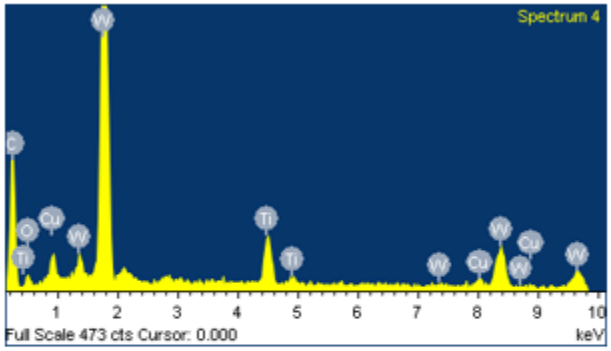

Element	Weight%	Atomic%
C K	42.75	83.50
O K	4.93	7.23
Ti K	5.63	2.76
Cu K	2.28	0.84
W M	44.41	5.67
Totals	100.00	

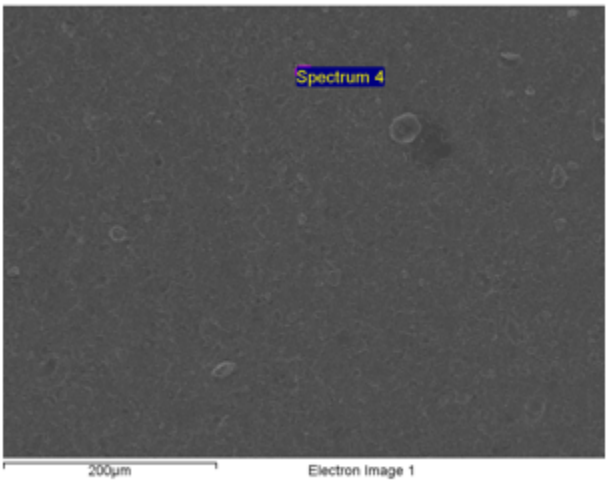

Table 4.1: (top) EDS results of material inside and outside main deposition area.

	Inside Main Deposition (at%)	Outside Main Deposition (at%)
Carbon	30.38	48.48
Tungsten	55.99	24.60
Titanium	8.70	22.74
Oxygen	3.09	3.41
Copper	1.83	0.76

Figure 4.10: Redeposition splatter observed in molybdenum discharge.

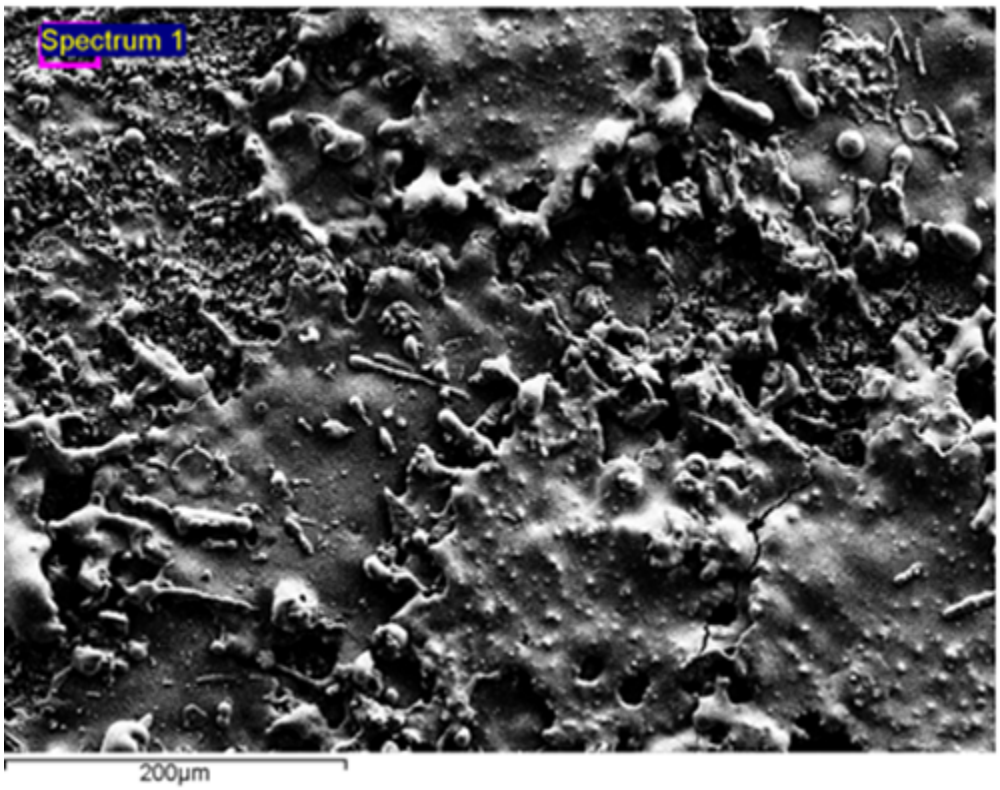

observed in these SEM images, it is likely that the material ejected from the device in the tungsten/lexan discharge becomes homogenized and/or chemically bound. This is reinforced by the relatively consistent tungsten percentage found within the bulk of the discharge.

Chapter 5

Summary, Conclusions and Future Work

Disruption events in future tokamak reactors which cause melting have the potential to significantly erode plasma facing materials, create unwanted aerosols or dusts, change surface properties, and contribute to accumulation of activated material. The divertor is a portion of the vacuum vessel which will be exposed to a large portion of this heat flux. The future large tokamak ITER will construct this component of tungsten. Experiments have been performed using the PIPE device to expose tungsten to disruption-like heat fluxes over appropriate time scales at small incidence angles. The goals of this work are to identify and quantify potential materials issues following a disruption like event, including amount of material ablated, melt layer formation and dynamics, void/bubble formation, cracking, and splashing.

This work has shown significant melting to occur under disruption-like conditions. For an incident heat-flux of 9.8 GW/m^2, a melt-layer forms and extends approximately 20 microns into the material bulk and experiences flow in the direction of the plasma wind. A large number of bubbles are observed in the melt-layer and there is significant surface cracking on the resolidified material. Large cracks which extend into the bulk are not observed. An average of 4 microns of material is ablated completely from the tungsten surface. Material splashing may or may not occur and needs to be investigated more fully.

Future experiments measuring the surface temperature of the tungsten during discharge will be useful in understanding the evolution of the melt-layer and formation of the resultant surface characteristics. Additional work is planned using helium plasmas as the incident ion source to better approximate fusion plasmas.

Bibliography

[1] "Fusion Electricity." A roadmap to the realisation of fusion energy. European Fusion Development Agreement. 2012.

[2] L., El-Guebaly. "Progressive Steps Towards Integral Nuclear Assessments for Fusion Devices." Transactions of the American Nuclear Society. 2013. 1151-1154.

[3] Jacquinot, J., et al. "Overview of ITER physics deuterium-tritium experiments in JET." Nuclear Fusion. Issue 39, V 2, 235 (1999): 235

[4] N. Sauthoff, et al., "Physics requirements for ITER engineering systems." In Proceedings of 16th IEEE NPSS Symp. Fusion Eng., Urbana Champaign, IL, 1, 130137 (1995)

[5] Burke, Dave. Toroidal coord. 2006. Graphic. Wikipedia. http://en.wikipedia.org/wiki/Torus

[6] EC-RTD-EURATOM. "Current tokamak sizes compared to ITER." Graphic. European Commission. http://ec.europa.eu/research/energy/euratom/index_en.cfm?pg=fusionion=prep-iter.

[7]Bolt, H., et al. "Materials for the plasma-facing components of fusion reactors."

Journal of nuclear materials 329 (2004): 66-73.

[8] Sugiyama, K., et al. "Tritium distribution on the surface of plasma facing carbon tiles used in JET." Journal of nuclear materials 313 (2003)

[9] Raffray, A. R., et al. "Breeding blanket concepts for fusion and materials requirements." Journal of nuclear materials 307 (2002)

[10] Rubel, M., et al. "Beryllium and carbon films in JET following DT operation." Journal of nuclear materials 313 (2003)

[11] Brooks, J. N., et al. "Analysis of C-MOD molybdenum divertor erosion and code/data comparison." Journal of Nuclear Materials 415.1 (2011): S112-S116.

[12] V. Barabash, G. Fediritci, R. Matera, A.R. Raffray, "The ITER Home Teams, Armour materials for the ITER plasma facing components." Physica Scripta T81, 7483 (1999)

[13] The ITER Divertor. Graphic. ITER.org. http://www.iter.org/mach/divertor

[14] G.E. Dale, M.A. Bourham, "Melt-layer erosion and resolidificationof metallic plasma-facing components." In Proceedings of 17th IEEE NPSS Symp. Fusion Eng., San Diego, CA, 2, 892895 (1997)

[15] A. Hassanein, I. Konkashbaev, "Theory and models of material erosion and lifetime during plasma instabilities in a tokamak environment." Fusion Eng. Design 5152, 681694 (2000)

[16] A. Hassanein, "Prediction of material erosion and lifetime during major plasma instabilities in tokamak devices." Fusion Eng. Design 60, 527546 (2002)

[17] J.P. Sharpe, M.A. Bourham, J.G. Gilligan, "Generation and characterization of carbon particulate in disruption simulation." Fusion Technol. 34, 634639 (1998)

[18] Stangeby, Peter. "The plasma boundary of magnetic fusion devices." ISBN: 978-0-7503-0559-4. Taylor and Francis, vol. 7 7 (2000).

[19] J.M. Linke, T. Hirai, M. Rodig, L.A. Singheiser, "Performance of plasma-facing materials under intense thermal loads in tokamaks and stellarators." Fusion Sci. Technol. 46, 142151 (2006)

[20] Mirnov et al, "Chapter 3: MHD stability, operational limits and disruptions," Nuclear Fusion, vol. 39, pp 2251 (1999)

[21] T. Hender et al., "Chapter 3: MHD stability, operational limits and disruptions" Nuclear Fusion, vol. 47, pp. S128S202, (2007)

[22] ITER Final Design Report complied by the ITER Director (2001)

(http://www.naka.jaea.go.jp/ITER/FDR/)

[23] G. Matthews et al., Steady-state and transient power handling in JET, Nuclear Fusion, vol. 43, pp. 9991005, (2003)

[24] Iwakiri, H., K. Morishita, and N. Yoshida. "Effects of helium bombardment on the deuterium behavior in tungsten." Journal of nuclear materials 307 (2002): 135-138.

[25] Roth, Joachim, et al. "Recent analysis of key plasma wall interactions issues for ITER." Journal of Nuclear Materials 390 (2009): 1-9.

[26] Rosanvallon, S., et al. "Dust limit management strategy in tokamaks." Journal of Nuclear Materials 390 (2009): 57-60.

[27] Arkhipov, N. I., et al. "Study of structure and dynamics of shielding layer for inclined incidence of plasma stream at MK-200 facility." Journal of nuclear materials 233 (1996): 767-770.

[28] Garkusha, I. E., et al. "Performance of deformed tungsten under ELM-like plasma exposures in QSPA Kh-50." Journal of Nuclear Materials 415.1 (2011): S65-S69.

[29] Sharpe, J. P., M. Bourham, and J. G. Gilligan. "Experimental investigation of disruption-induced aerosol mobilization in accident scenarios of ITER." Fusion Engineering, 1997. 17th IEEE/NPSS Symposium. Vol. 1. IEEE, (1997)

[30] Gilligan, John, and Mohamed Bourham. "The use of an electrothermal plasma gun to simulate the extremely high heat flux conditions of a tokamak disruption." Journal of fusion energy 12.3 (1993)

[31] G.E. Dale, M.A. Bourham, "Experimental investigation into meltlayer erosion of plasma-facing materials." Fusion Technology 34, 901907 (1998)

[32] L. Winfrey, J. Gilligan, A. Saveliev, M. Abd Al-Halim, M. Bourham, "A study of plasma parameters in a capillary discharge with calculations using ideal and non-ideal plasma models for comparison with experiment." IEEE Trans. Plasma Science 40, 843852

(2012)

[33] Edamitsu, Toshiaki, and Hirokazu Tahara. "Experimental and numerical study of an electrothermal pulsed plasma thruster for small satellites." Vacuum 80.11 (2006)

[34] Dyvik, Jahn, et al. "Recent activities in electrothermal chemical launcher technologies at BAE systems." Magnetics, IEEE Transactions on 43.1 (2007)

[35] Kincaid, R. W., and M. A. Bourham. "Electrothermal plasma gun as a pellet injector." Fusion technology 26.CONF-940630– (1994).

[36] Gebhart, T. E., et al. "Optimization of Fusion Pellet Launch Velocity in an Electrothermal Mass Accelerator." Journal of Fusion Energy (2013)

[37] Echols, J. R., et al. "Evaluation of materials deposited by a novel electrothermal plasma technique." Pulsed Power Conference (PPC), 2013 19th IEEE. IEEE, (2013).

[38] Hassanein, A., and I. Konkashbaev. "Lifetime evaluation of plasma-facing materials during a tokamak disruption." Journal of nuclear materials 233 (1996): 713-717.

[39] Gilligan, J., D. Hahn, and R. Mohanti. "Vapor shielding of surfaces subjected to high heat fluxes during a plasma disruption." Journal of Nuclear Materials 162 (1989)

[40] Hassanein, A. M., G. L. Kulcinski, and W. G. Wolfer. "Surface melting and evaporation during disruptions in magnetic fusion reactors." Nuclear Engineering and Design. Fusion 1.3 (1984)

[41] Kim, Kyoungjin. "Time-dependent one-dimensional modeling of pulsed plasma

discharge in a capillary plasma device." Plasma Science, IEEE Transactions on 31.4 (2003)

[42] Hassanein, Ahmed, A. Konkashbaev, and I. Konkashbaev. "Erosion of melt layers developed during a plasma disruption." Presented at the 18th European Symposium on Fusion Technology, Karlsruhe, Germany, 22-26 Aug. 1994. Vol. 1. 1994.

[43] Miloshevsky, G., and Ahmed Hassanein. "Modeling of macroscopic melt layer splashing during plasma instabilities." Journal of Nuclear Materials 415.1 (2011): S74-S77.

[44] Hassanein, A., and I. Konkashbaev. "Comprehensive physical models and simulation package for plasma/material interactions during plasma instabilities." Journal of nuclear materials 273.3 (1999): 326-333.

[45]Nishijima, Dai, et al. "Formation mechanism of bubbles and holes on tungsten surface with low-energy and high-flux helium plasma irradiation in NAGDIS-II."Journal of nuclear materials 329 (2004): 1029-1033.

[46] Coenen, J. W., et al. "Tungsten melt layer motion and splashing on castellated tungsten surfaces at the tokamak TEXTOR." Journal of Nuclear Materials 415.1 (2011): S78-S82.

[47] Nishijima, Dai, et al. "Formation mechanism of bubbles and holes on tungsten surface with low-energy and high-flux helium plasma irradiation in NAGDIS-II."Journal of nuclear materials 329 (2004): 1029-1033.

[48]Kajita, Shin, et al. "Formation process of tungsten nanostructure by the exposure to helium plasma under fusion relevant plasma conditions." Nuclear Fusion 49.9 (2009):

095005.

[49] Bazylev, Boris, et al. "Experimental and theoretical investigation of droplet emission from tungsten melt layer." Fusion Engineering and Design 84.2 (2009): 441-445.

[50] Klimov, N., et al. "Experimental study of PFCs erosion under ITER-like transient loads at plasma gun facility QSPA." Journal of Nuclear Materials 390 (2009): 721-726.

[51] Hassanein, A., and I. Konkashbaev. "Performance and lifetime assessment of reactor wall and nearby components during plasma instabilities." Journal of nuclear materials 258 (1998): 645-652.

[52] Hassanein, Ahmed, A. Konkashbaev, and I. Konkashbaev. "Erosion of melt layers developed during a plasma disruption." Presented at the 18th European Symposium on Fusion Technology, Karlsruhe, Germany, 22-26 Aug. 1994. Vol. 1. 1994.

[53] Compan, J.,s et al. "Reduction of preferential erosion of carbon fibre composites under intense transient heat pulses." Physica Scripta 2007.T128 (2007): 246.

[54] Linke, J., et al. "Erosion of metals and carbon based materials during disruption-ssimulation experiments in plasma accelerators." Journal of nuclear materials 212 (1994): 1195-1200.

[55] Majerus, Patrick, et al. "The new electron beam test facility JUDITH II for high heat flux experiments on plasma facing components." Fusion engineering and design 75 (2005): 365-369.

[56] Arkhipov, N. I., et al. "Material erosion and erosion products in disruption simulation experiments at the MK-200 UG facility." Fusion engineering and design 49 (2000): 151-156.

[57] Powell, John D., and Alexander E. Zielinski. Theory and experiment for an ablating-capillary discharge and application to electrothermal-chemical guns. No. BRL-TR-3355. Army ballistic research lab aberdeen proving ground MD (1992)

[58] Cuperman, Sami, et al. "Consistent treatment of critical plasma flows in high pressure discharge ablative capillaries." Plasma Science, IEEE Transactions on 21.3 (1993)

[59] Amelinckx, S., Electron microscopy: principles and fundamentals. Weinheim: Print.

[60] Wittke, James. "Instrumentation." Northern Arizona University, 2008. Web. ¡http://www4.nau.edu/microanalysis/Microprobe-SEM/Instrumentation.html¿.